Master in Quantum Science and Technology

Scanning tunneling microscope for nanoscale photon spectroscopy: Study of novel transition metal dichalcogenide - nanoporous graphene heterostructures

Marina Isabel de la Higuera Domingo

Supervisors:

Dr. Marc González Cuxart

Prof. Aitor Mugarza

Atomic Manipulation and Spectroscopy Group
Catalan Institute of Nanoscience and Nanotechnology

July, 2024

Universitat de Barcelona

UAB
Universitat Autònoma de Barcelona

UPC
Universitat Politècnica de Catalunya
BarcelonaTech

To my family and my beloved ones.

Scanning tunneling microscope for nanoscale photon spectroscopy: Study of novel transition metal dichalcogenide - nanoporous graphene heterostructures

Marina Isabel de la Higuera Domingo

Supervised by: Dr. Marc González Cuxart, Prof. Aitor Mugarza.

Atomic Manipulation and Spectroscopy group, ICN2-Catalan Institute of Nanoscience and Nanotechnology, UAB Campus, 08193 Bellaterra, Barcelona (Spain).
15 July 2024

The development of Scanning Tunneling Microscopy (STM) techniques represents one of the most significant advances in modern materials science. By enabling the observation and manipulation of structures at the atomic scale, STM techniques open up a field of study previously unattainable to other imaging and spectroscopic methods. For instance, light-matter interaction research was significantly limited by the Abbe diffraction limit in conventional optical spectroscopy. The introduction of quantum mechanics principles in microscopy technologies has provided new approaches to overcome these obstacles, allowing investigations such as controlling excitons behaviour in 2D semiconductors. Excitons, which have a significant impact on material behaviour, offer broad applications in optoelectronic devices, including new platforms of interacting qubits or superlattices of interacting single quantum emitters.

This work addresses the principles and techniques of STM applied in photoluminescence studies (Photon-STM). The primary focus lies on the detailed development of an experiment conducted in collaboration with the Photon-STM group of Prof. Martin Švec to characterize excitons in $MoSe_2$. This involves a comprehensive range of challenging tasks, from sample preparation to detecting excitonic phenomena, with my active participation in every stage of the process. This study serves a dual purpose: it documents the experimental procedures, covering prior sample preparation, obtained results and future prospects; and it provides a thorough analysis of the Photon-STM optical setup. In parallel, the difficulties encountered in commissioning a Photon-STM microscope at ICN2 and first preliminary results are presented in an appendix.

Keywords: STM, PSTM, TMD, NPG, PL, TEPL, Raman

Contents

Acronyms

AFM	Atomic Force Microscopy
BL	Bilayer
CCD	Charge Coupled Device
DOS	Density of States
EM	Electromagnetic
FER	Field Emission Resonance
FF	Far-Field
FIB	Focused Ion Beam
GNR	Graphene Nanoribbon
IPS	Image Potential States
LDOS	Local Density of States
LSP	Localized Surface Plasmon
LT	Low Temperature
ML	Monolayer
NF	Near-Field
NPG	Nanoporous graphene
PDMS	Polydimethylsiloxane
PL	Photoluminescence
PSTM	Photon-STM
SERS	Surface-Enhanced Raman Spectroscopy
SPM	Scanning Probe Microscopy
STM	Scanning Tunneling Microscopy
STML	STM-Induced Luminescence
STS	Scanning Tunneling Spectroscopy
TEPL	Tip-Enhanced Photoluminescence
TERS	Tip-Enhanced Raman Spectroscopy
TIP	Tip-Induced Plasmon
TL	Trilayer
TMD	transition-metal dichalcogenide
UHV	Ultra High Vacuum

1 Introduction

As Richard P. Feynman predicted in his 1959 lecture “There is plenty of room at the bottom” [Fey60], the development of nanoscale devices has revolutionised the field of materials science. He foresaw that observing and manipulating individual atoms would lead to the discovery of novel material properties and technological advances. It was not until 20 years later that his vision materialized with the invention of the Scanning Tunneling Microscopy (STM) in 1982 and the Atomic Force Microscopy (AFM) in 1986. They paved the way for other Scanning Probe Microscopy (SPM) [KSB+16] techniques, which enable the imaging and manipulation of material structures at the nanoscale. This transformed Feyman’s foresight into a vast field of research: nanoscience and nanotechnology.

Driven by the limitations of conventional bulk materials in device performance [GMR+17], research has increasingly focused on low-dimensional quantum materials. They offer unique properties arising from quantum mechanics, enabling customization and miniaturization for enhanced functionality. While STM has long been pivotal for atomic-scale studies, its capabilities are being expanded through the integration of other complementary techniques such as optical spectroscopies. This combination, known as Photon-STM (PSTM), requires well-controlled ultra-high vacuum (UHV) environments and cryogenic temperatures to reach atomic spatial resolution. These also minimize surface contamination, thermal noise, diffusion, and drift. Notably, PSTM transcends traditional STM by allowing the study of light-matter interactions at the nanoscale, including localized fluorescence, charge carrier dynamics, and light absorption, emission, and conversion processes. These insights are crucial for optimizing energy conversion efficiency and unlocking superior performance of optoelectronic devices.

Optical spectroscopy is essential for probing condensed matter’s electronic and photophysical characteristics. However, conventional far-field (FF) techniques are not suitable for nanoscale investigations due to diffraction-limited spatial resolution and low sensitivity. To address these challenges, near-field (NF) imaging was proposed in 1928 and later implemented using STM in 1988 by Gimzewski and coworkers [GRCS88]. Although STM does not allow access to optical information, its precise control over tip-sample separation, together with the requirement of proximity to achieve non-diffraction-limited resolution, has promoted its combination with this NF approach. The STM tip operates at an extremely close distance to the sample surface, bypassing wavelength-imposed limitations on resolution. This proximity allows the tip to sense the electron cloud of the sample atoms rather than relying on light diffraction patterns. Additionally, when light interacts with a subwavelength aperture, it creates localized, non-propagating evanescent waves that decay exponentially with distance. In NF imaging, these evanescent waves strongly interact with the sample, allowing for multifunctional nanocharacterizations with high spatial resolution and sensitivity. This has led to effective techniques such as Tip-Enhanced Photoluminescence (TEPL) and STM-induced luminescence (STML) nanospectroscopy [LRS+23].

This project reports the experimental study of electron-hole pairs (excitons) in 2D heterostructures [JNB+23]. The focus lies on few-layer $MoSe_2$ deposited on nanoporous graphene (NPG) with an Au(111) substrate underneath. This unprecedented layered heterostructure allows the exploration of exciton spatial confinement in the superlattice potential that the NPG imposes on the otherwise continuous $MoSe_2$. The related activity involves the preparation and realization of an experiment in which the aforementioned sample is excited with a laser light source to study its luminescence properties using TEPL and STML techniques. It also investigates the engineering and control of excitons in a 2D semiconductor [KMI+19], which can provide a platform of interacting qubits or a superlattice of interacting single quantum emitters, and also promote superradiance or Bose-Einstein condensation. Excitons are crucial for understanding light absorption and emission of quantum materials and their applications in new electronic devices such as photodetectors, solar cells and light-emitting diodes (LEDs) [IMII+17]. For instance, in photodetectors, exciton transport and recombination processes dictate the device's sensitivity and response speed. Furthermore, for photovoltaic cells, their dissociation dynamics determine the device's power conversion efficiency.

Recent advances in PSTM have enabled the exploration of exciton generation mechanisms at the single molecule or atomic defect level [DCMv21b, DCMv21a, DMN+20]. To this end, several samples were prepared at ICN2 laboratories and analyzed in collaboration with the Photon-STM group of Prof. Martin Švec (Institute of Physics, Czech Academy of Sciences, Prague) using a Low Temperature (LT)-STM setup specifically configured for photoluminescence experiments. In addition, at the end of this work, a technical section will illustrate the assembly and calibration of a non-commissioned STM in the ICN2 labs, emphasizing the complexity of achieving proper functionality and atomically-resolved imaging. This comprehensive report aims to support future research in the field, providing insights and practical guidelines for advancing nanoscale optical investigations with PSTM.

2 Experimental Techniques

This chapter presents the main experimental techniques employed in this thesis. The first section is dedicated to Scanning Tunneling Microscopy (STM) and Spectroscopy (STS), which enable tracking the topography and the electronic structure of a material *in-situ* with sub-nm resolution. The second section introduces non-local optical techniques and, finally, the third part briefly describes the Photon-STM (PSTM) microscopes used to detect the sample's optical response.

2.1 Scanning Tunneling Microscopy (STM)

Invented by Gerd Binniga and Heinrich Rohrer in 1981, Scanning Tunneling Microscopy was the first scanning probe technique to allow the study and manipulation of materials at the atomic scale. In STM, a metallic tip with a single-atom apex is positioned approximately 10 Å away from a conductive sample surface [Che07]. This close proximity allows electrons to tunnel through the STM junction due to the wave-like nature of electrons, a phenomenon known as the quantum tunneling effect. By applying a voltage between tip and sample, a finite tunneling current is then generated. The existing dependence of this current on the tip-sample distance characterizes the functionality and operation of STM in two primary modes: constant current mode and constant height mode. In the former, the distance between tip and sample is adjusted by a feedback loop to maintain a current set-point, while the z displacement of the piezo is recorded and represents the topographic height. In the latter, the tip-sample separation is fixed, and the variations in the

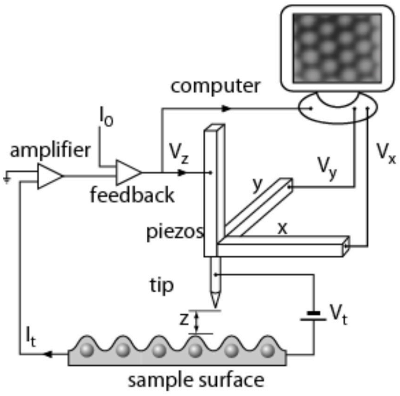

Figure 1: Operation of an STM in constant current mode: A bias voltage between tip and sample induces a tunneling current. A feedback system controls the z piezo to maintain a constant current during a scan. Image taken from [Che07].

tunneling current are measured, representing the topographic height. For this work, the STM will always operate in constant current mode, as it is more convenient for scanning large regions without the risk of crashing the tip.

2.1.1 STM Working Principle: Quantum Tunnelling

According to classical mechanics, an electron moving in a region with a potential barrier cannot pass through it unless its initial energy exceeds the barrier's height. However, in quantum mechanics, there is a certain probability for the particle to cross the barrier even when its initial energy is lower than the potential height. The propagation of an electron, described by a wavefunction $\psi(z)$ (wave-particle duality), across a potential barrier is determined by the stationary solutions of the time-independent Schrödinger equation in one dimension:

$$\left[-\frac{\hbar^2}{2m}\frac{\partial^2}{\partial z^2}+V(z)\right]\psi(z)=E\,\psi(z). \tag{1}$$

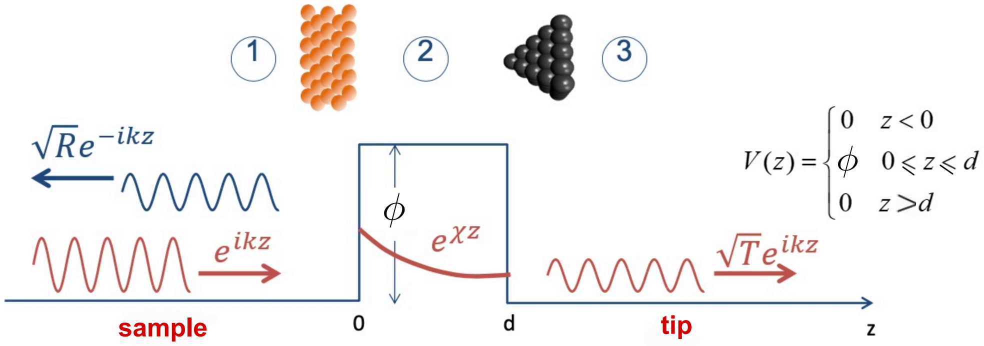

Figure 2: Quantum tunneling in the sample-tip junction: the particle can tunnel the potential barrier even when its initial energy is lower than the potential height. An incident and a reflected wavefunction are depicted at the left side of the barrier, the evanescent wave inside it and the transmitted wave on the other side. This potential barrier in the STM junction is modulated by the tip-sample distance. Image taken from [GW93].

The solutions for the electronic wavefunction within the STM junction modeled as a barrier potential (Figure 2), for $E < \phi$, are as follows:

$$\psi(z)=\begin{cases}\mathrm{A}_1e^{ikz}+\mathrm{A}_2e^{-ikz} \quad \text{if} \quad z<0 \quad \text{region 1: Incident and Reflected}\\ \mathrm{B}_1e^{\chi z}+\mathrm{B}_2e^{-\chi z} \quad \text{if} \quad 0\le z\le d \quad \text{region 2: Evanescent}\\ \mathrm{C}e^{ikz} \quad \text{if} \quad z>d \quad \text{region 3: Transmitted}\end{cases}, \tag{2}$$

where

$$k=\frac{\sqrt{2m\mathrm{E}}}{\hbar}>0, \qquad \chi=\frac{\sqrt{2m(\phi-\mathrm{E})}}{\hbar}>0. \tag{3}$$

Constant parameters A_i,B_i with $i=1,2$ and C can be determined by applying boundary conditions (see reference [Che07]). Assuming[1] $\phi \gg E$, the tunneling current is proportional to the probability that an electron from the sample is at the tip position d:

---

[1] In this model, ϕ represents the work function of the material. For metals, the Fermi level is around 5 eV below the vacuum level, this difference defining the work function. Since the tunneling electron energy E is close to the Fermi energy, it is easy to see that $E \ll \phi$.

$$I \propto |\psi(d)|^2 \propto e^{-2\chi d} \sim e^{-2\frac{\sqrt{2m\phi}}{\hbar}d}. \tag{4}$$

Nevertheless, this simplified model does not capture all the phenomena occurring in the junction. The tunneling current also depends on intrinsic properties such as the local density of states (LDOS), number of states per unit energy, of sample and tip and the Fermi-Dirac distribution, which describes the occupancy of electron states. This is the reason why, in constant current mode, STM measures constant lines of the LDOS rather than just topography.

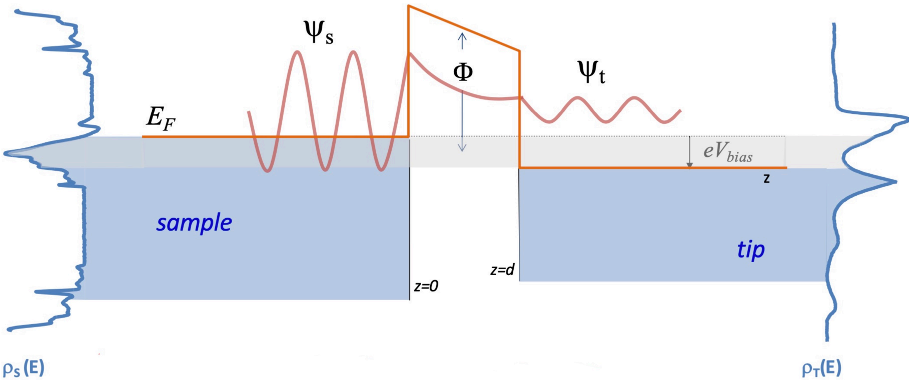

Figure 3: Potential energy diagram illustrating the tunneling process between tip and sample. The grey region represents the overlapping energy area, with occupied states (blue region) on one side and unoccupied states (white region) on the other side. When a negative bias voltage is applied, electrons tunnel from the occupied states in the sample to the unoccupied states in the tip. If the applied bias voltage is positive, the electrons will flow from the occupied states of the tip into the empty states of the sample. Image taken from [GW93].

Considering more realistic models (Figure 3) that include electronic structure effects, such as the one proposed by Tersoff and Hamann in 1983 [Che07], the tunneling current in the low-temperature limit can be expressed as

$$I = \frac{4\pi \mathrm{e}}{\hbar} \overbrace{\mathrm{e}^{-2\frac{\sqrt{2m\phi}}{\hbar}d}}^{\text{Spatial sensitivity}} |M^*|^2 \int_0^{\mathrm{eV}} \overbrace{\rho_S\left(E_F + \epsilon - \mathrm{eV}\right)}^{\text{Spectroscopic sensitivity}} \rho_T\left(E_F + \epsilon\right) d\epsilon. \tag{5}$$

Symbol	Notation
$\rho_{S,T}$	DOS of sample and tip
eV	Applied bias voltage
E_F	Fermi energy level
ϕ	Work function
M^*	Tunneling matrix element

Table 1: Parameters notation.

According to expression (5), the tunneling current depends on the tip-sample distance and the integral of the convoluted density of states (DOS) of tip and sample in the energy range from the Fermi level to the applied bias voltage (grey region in Figure 3).

2.1.2 Scanning Tunneling Spectroscopy (STS)

Shortly after the initial demonstration of STM, theoretical analysis of electron tunneling through a vacuum barrier showed that the current depends on the LDOS of both sample and tip (equation (5)). Scanning Tunneling Spectroscopy (STS) was developed (1982) to probe the LDOS and the gap of a sample to obtain information about its conducting, semiconducting or insulating nature [Voi15]. Since the spectroscopic information is acquired from both tip and sample, this procedure requires a metallic tip with a relatively flat DOS near the Fermi level. In consequence, the convolution of the LDOS measured by STS can be approximated as proportional to the sample LDOS.

STS is typically carried out by measuring the tunneling current variations as a function of voltage (differential conductance, $\mathrm{d}I/\mathrm{d}V$) on a specific spot of the sample under open feedback-loop conditions. The differential conductance can be obtained numerically from the measured $I(V)$, however, using a lock-in amplifier leads to a higher signal-to-noise ratio and a wider dynamic range. A small harmonic modulation with a specific frequency is applied to the bias voltage and the corresponding modulation-related signal, which is proportional to $\mathrm{d}I/\mathrm{d}V$, is extracted via a lock-in technique. Lock-in measurements provide signals within a defined frequency band around the reference frequency, rejecting all other components. This allows for accurate detection even in the presence of noise up to a million times higher in amplitude. [Loc23]

Assuming then that the transmission factor and the tip DOS are slowly varying functions of energy, the tunnelling current is evaluated by summing over all relevant sample states. Thence, the differential conductance, calculated by taking the derivative of equation (5), is directly proportional to the sample LDOS at the applied bias voltage,

$$\frac{dI}{dV}(V,\vec{r}) \propto \rho_S(eV). \tag{6}$$

The $\mathrm{d}I/\mathrm{d}V$ signal can be acquired through the local spectroscopic technique STS by sweeping the bias voltage to get ρ_S at a specific position and as a function of energy. When STS is combined with STM, it creates a unique tool that enables the mapping of a material's LDOS at the atomic level. This allows researchers to study a wide range of spectroscopic features, including molecular orbitals, crystal defect states, quantum interference phenomena, inelastic transitions associated with molecular or lattice vibrations, spin transitions, etc.

2.2 Non-local optical spectroscopic techniques

2.2.1 Raman spectroscopy

Raman spectroscopy is a two-photon process widely used to study optically active inelastic excitations in materials. Raman effect involves inelastic photon scattering, where the energy transferred between light and material corresponds to the energy of a particular excitation (such as phonons, plasmons, magnons, etc.).

When a sample is illuminated with a monochromatic source, most of the light is elastically scattered (Rayleigh scattering), *i.e.*, the outcome beam has the same characteristics (wavelength, frequency, colour) as the incoming one. However, a small fraction of photons transfers part of their energy to the sample, a phenomenon termed as inelastic or Raman scattering. Focusing on the most commonly studied excitations, which are vibrations, the inelastically scattered light will exhibit a frequency reduction equal to the specific energy quanta absorbed by the excited vibrational mode. Collecting Raman scattered light allows then to determine the structural information of a sample, enabling to map a Raman spectrum of the material. [Zha21]

However, Raman scattering is an extremely attenuated phenomenon, as it is a third-order interaction process[2]. To detect these weak signals, a Charge Coupled Device (CCD) is typically used in a Raman setup. A multichannel CCD can collect more scattered light signals in a shorter time compared to a common photomultiplier tube [SDR05], enhancing detection efficiency.

2.2.2 Photoluminescence (PL)

Whereas Raman scattering probes electron-lattice interactions, photoluminescence (PL) spectroscopy is directly related to the electronic band of a material. It is a well-known technique for studying luminescent properties of semiconductors [ZFR+06]. Luminescence, the spontaneous emission of light from an electronically or vibrationally excited state, not necessarily due to a thermal source, occurs in various natural and artificial materials, revealing the energetic interplay between light and matter. PL provides insights into light absorption, emission and energy transfer mechanisms, such as recombination and quantum efficiencies, as well as the effects of external factors like defects. In a typical PL experiment, the material is excited with a monochromatic light source with photon energy greater than the bandgap (photoexcitation). As excited electrons return to equilibrium, the energy is released either as light (radiative) or through other non-radiative processes. The emitted light is then collected and analyzed as a function of wavelength by a spectrometer.

Lasers are commonly used for PL excitation due to their monochromatic, intense, and focused beam. The intensity and energy of the emitted light in PL strongly depend on the material's electronic band structure, making PL a contactless, non-destructive method of probing its electronic properties. This technique is particularly effective for investigating two-dimensional (2D) materials, due to their intrinsic electronic properties, and for detecting low concentration of optical centres. However, it also possesses several restrictions including limited spatial resolution [LLK+20].

2.3 Optical spectroscopic techniques combined with STM

Crystalline solids exhibit specific surface features dictated by the lattice periodicity. However, minor imperfections can distort this spatial arrangement, creating localized defect states which can serve as charge-trapping centers and pinning sites. In addition, defects and atomic-scale disorder can lead to the coexistence of multiple crystal phases within a few nanometers, causing the material's local response to external perturbations to vary significantly over incredibly small distances [GGA+21]. Understanding how these microscopic interactions and non-equilibrium dynamics fluctuate around local defects or across multiple nanometer-sized domains is crucial for both fundamental research and nanotechnology applications.

To gain deeper insights into these microscopic interactions related to light-matter coupling and to local optical responses of materials, Photon-STM (PSTM) was developed in the late 1980s [Sto11]. In a standard STM, the current flowing between tip and sample can induce electroluminescence from the junction. PSTMs specifically exploit this phenomenon by incorporating optical components such as lenses and mirrors, positioned near the tunnel junction to maximize the collection of emitted light.

---

[2] The inelastic scattering of an incident photon by phonos in a crystal is defined by a third-order interaction process involving electron-radiation and electron-lattice interactions [JHZ+19].

2.3.1 Plasmon Nanocavity

Many different approaches have been developed to integrate or extract light within the STM junction. A pivotal element in these techniques is the role of field enhancement at the STM tip, which results from the geometric confinement of electromagnetic (EM) energy [HLC+11]. The coupling of EM radiation with matter arises through interactions with charge carriers (electrons and holes) within the junction, resulting in processes similar to those used in spectroscopy techniques. These interactions include four main mechanisms: (1) light-induced tunneling, in which external light lowers the tunneling barrier inducing a current between tip and sample; (2) inelastic tunneling, characterized by the interaction of tunneling electrons with EM radiation, leading to photon absorption or emission and subsequent light generation; (3) light-generated excitations, where the incoming light induces localized excitations (such as molecules, defects, or nanostructures) in entities within the STM junction; and (4) radiative decay of excitations, excited states generated by tunneling processes decay radiatevely emitting photons. [DVK+10]

Field emission enhancement in these nanocavities provides spatial resolution limited to the probing size of the tip and generates an intense enough signal to study single nanometric entities [LWK18]. This arises from the localization of EM fields at the tip apex due to the electrons' collective resonant oscillation when a laser beam is applied (localized surface plasmon[3] LSP resonance effect). The presence of a plasmonic tip near an emitter enhances the sample's spontaneous emission rate, a phenomenon known as the Purcell effect [KSS+15]. This combined enhancement of excitation and emission rates because of a plasmonic tip results in a significantly stronger emission signal.[MJFDL+20]

2.3.2 STM-induced luminescence (STML)

STM-induced luminescence (STML) relies on the energy transfer between electrons and photons through two major processes illustrated in Figure 4. As shown in Figure 4**(b)**, plasmonic emission is the emission of light from an inelastic electron tunnelling event which directly excites a tip-induced plasmon (TIP) that decays emitting a photon. In contrast, an active medium in between sample and tip may accompany these interactions as shown in Figure 4**(c)**, deriving in excitonic emission. As both tip and sample can be excited by charge injection, excitons in semiconductors or luminescent molecules will form and subsequently recombine radiatively.[ROC+19]

2.3.3 Tip-Enhanced Photoluminescence (TEPL)

TEPL [YCG+20] represents a feasible alternative for nanoscale analysis of electronic and optical properties with high spatial resolution (below 1 nm) and sensitivity due to the plasmonic antenna effect, also referred to as lightning rod effect. It provides insight into the electronic properties of materials at the atomic scale, such as TMDs, quantum dots and quantum wires. In a TEPL experiment, a laser is focused at the STM junction, exciting the LSP at the tunneling nanocavity. When the LSP and the excitation laser wavelengths overlap (resonance), a huge enhancement of the EM field occurs at the apex because of the Purcell effect [KSS+15], increasing the PL from the region immediately below the tip and enabling mapping of PL with nanoscale resolution. [MJFDL+20]

---

[3] In the context of STM, plasmons refer to the collective electron oscillations at the interfaces of metallic nanostructures (sample or/and tip).

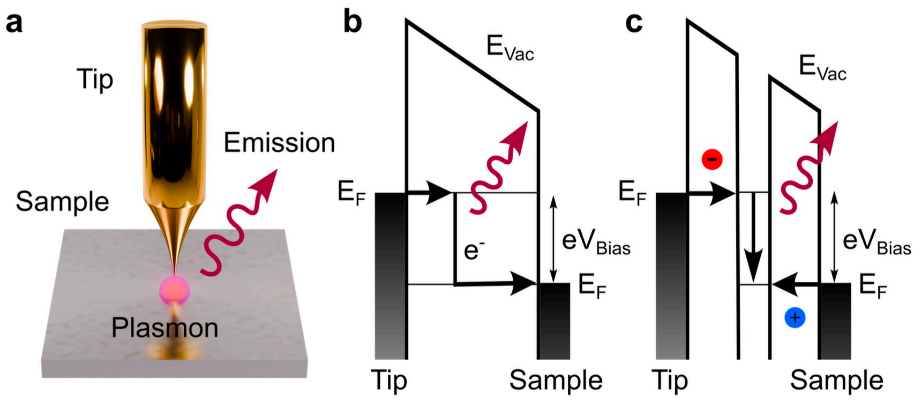

Figure 4: **a)** Scheme of electroluminescence in the STM. The tip is brought into the tunneling regime and maintained at a constant distance from the sample surface. **b)** and **c)** energy band diagram for the two mechanisms, plasmonic and excitonic emission respectively, that induce luminescence in the junction. The DOS of both tip and sample are depicted considering constant occupation up to the Fermi energy. They are shifted by the energy difference eV_{Bias}, induced by the bias voltage. E_{Vac} represents the vacuum energy level. In **b)**, the inelastic process involves a tunneling electron travelling from the tip to the sample, exciting a tip-induced plasmon mode. Once the plasmon is excited, it decays radiatively, emitting a photon in the process. In **c)**, the energy levels of the excitonic states formed in the junction are presented. The photonic emission in this case is due to the recombination of electrons and holes (excitons) in the junction. Image taken from [Sch24].

2.3.4 Tip-Enhanced Raman Spectroscopy (TERS)

Since its foundation in 1974 by Fleischmann, Surface-Enhanced Raman Spectroscopy (SERS) has been used in various fields. SERS intensifies the Raman spectrum through two main mechanisms: electric field and chemical enhancement. In the first case, LSP resonances of roughened or nanostructured metallic surfaces are used to greatly amplify the inherently weak Raman scattering signal. In contrast, the second process involves changes in the electronic structure of molecules adsorbed on metal surfaces, leading to selective enhancement of certain Raman peaks [FHM74]. Although SERS overcomes the limitation of low Raman scattering cross section, its spatial resolution is still restricted by the excitation wavelength due to the diffraction limit. Moreover, distinguishing whether a Raman signal originates from target molecules, contaminants, or decomposition products is challenging with this technique because of their coexistence at the nanometric scale. To address these constraints, Tip-Enhanced Raman Spectroscopy (TERS) was developed combining the advantages of Raman spectroscopy and SPM [CS22]. TERS achieves an increased spatial resolution by using a sharp metal tip while maintaining the enhancement factor necessary for detecting subnanoscale objects. When a focused laser illuminates the apex of the metal tip, the LSP around the tip apex is excited and, as it approaches the substrate, a hot spot is created in the gap between tip and sample. Raman signals from this spot are largely enhanced and scattered to the far field [ZSWS16].

3 STM Plasmonic Tips

Previously discussed PSTM requires a tip with specific characteristics, which influence both its preparation and its interaction with the material under study. For most STM techniques, the tip apex must end in a single atom, creating a single tip-sample junction through which tunneling dominates. In the case of STS, the tip should possess a featureless (metallic) electronic structure to ensure that the $\mathrm{d}I/\mathrm{d}V$ spectra represent the LDOS of the sample without convolution from tip states. For luminescent techniques requiring the assistance of a LSP (TERS and TEPL spectroscopy), materials such as Ag and Au are commonly used due to their low losses in the visible and infrared range, as their plasmonic modes are typically centered at these energies.[PGB20]

3.1 Tip fabrication

3.1.1 Principles of Chemical Etching

Electrochemical etching is a widely used technique for fabricating STM tips. It involves a reduction-oxidation reaction where a metal is oxidized by an etching reagent. For future PSTM experiments at ICN2, Au tips will be fabricated using hydrogen chloride (HCl) as the etchant. Au is an ideal candidate for a plasmonic base material due to its manageable etching properties compared to other noble metals [Sch24]. The process initiates by applying a voltage potential, deriving in the following chemical reactions:

$$\text{Gold oxidation:} \qquad \mathrm{Au_{(s)} + 4Cl^-_{(aq)} \rightarrow [AuCl_4]^-_{(aq)} + 3e^-}, \tag{7}$$

$$\text{Reduction of HCl:} \qquad \mathrm{Au_{(s)} + 2Cl^-_{(aq)} \rightarrow [AuCl_2]^-_{(aq)} + e^-}. \tag{8}$$

Au wire with a diameter of 0.25 mm is immersed into the etching solution, where capillary forces yield the formation of a meniscus around it (setup in Appendix D.1, Figure 29). As the wire thins, its tensile strength decreases until it can no longer sustain the weight of its lower end, leading to its breakage and leaving a sharp tip behind [Luc04]. This is commonly known as the "drop-off" method (Figure 5).

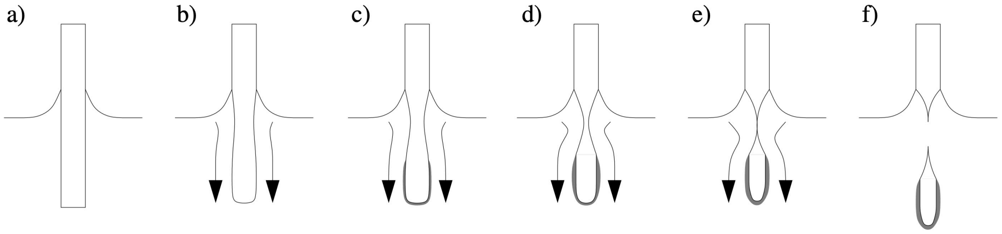

Figure 5: Drop-off method **a)** Formation of the meniscus. **b)** to **e)** Flow of the solution towards the lower end of the wire, the creation of a dense layer around the bottom of the wire and the necking phenomenon in the meniscus. In **f)**, the lower part breaks off. Image taken from [Luc04].

The etching process depends on a variety of parameters (applied voltage, solution composition, etc.), and optimizing them is crucial for obtaining suitable Au tips. An ideal tip has a cone shape at the micrometre scale with a sharp end. A rough tip favours radiation coupling at multiple surface points (lightning-rod effect), causing interference and reflections within the nanocavity [Luc04]. Surface irregularities may also introduce uncertainties in optical excitation measurements, even at significant distances from the sample.

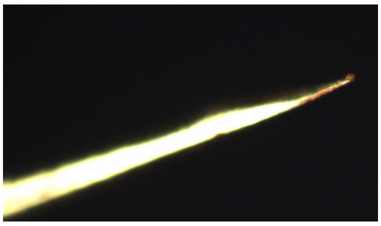

Figure 6: Final result of the etched Au tip for the PSTM setup at ICN2. Voltage : 3.5V, Time: 40 min, Etchant: HCl 37%, Diluent: Ethanol. Solution: 75% HCl, 25% Ethanol.

The composition and contact area of the etching solution significantly affect the outcome. The etchant (HCl) concentration determines the reaction speed once a voltage is applied. A fast reaction increases disturbances in the solution, interfering with the etching process. Therefore, it is necessary to decrease the concentration of HCl by adding a diluent, such as ethanol, to stabilize the meniscus. Nevertheless, too much diluent may hinder the reaction by creating a thin oxidation layer at the meniscus and depositing unwanted compounds on the tip's surface (Appendix D.1, Figure 30). Thus, finding the right balance between the etchant and the diluent is critical (final result in Figure 6).

3.2 Ultra High Vacuum (UHV) *in-situ* tip preparation

UHV *in-situ* preparation refers to the process of cleaning and sharpening the tip within the same UHV chamber of the STM to achieve a sharp tip apex at the last few atoms scale. Even though the tip fabrication techniques previously discussed are designed to optimize the tip's shape and conserve the integrity of the junction, multiple tunneling pathways can still exist between tip and sample at the nanometer-scale apex. These pathways, including adsorbates and local surface corrugations, often manifest as current instabilities, "ghost" images or replicas of topographic features. In this context, *in-situ* means to perform the tip treatment within the UHV chamber, minimizing the risk of contamination from exposure to air or other external factors. Once the tip is in tunneling conditions, there are mainly two approaches for cleaning and sharpening the tip: voltage pulses and indentations. Typical parameters for these processes are voltage pulses ranging from -10 to 10 V and indentations ranging from 1 to 40 nm, which can be performed with or without bias.

3.2.1 Plasmonic Tip

An optically active and atomically sharp Ag-tip was prepared by electrochemical etching and focused ion beam (FIB) (see Appendix A) to conduct the excitons' experiment in Prague. Controlled indentations and voltage pulses were also applied to obtain a strong plasmonic response of high intensity (Figure 7 **(b)**), with an emission spectrum overlapping the energy of the excitation source and the emission lines under study (Figure 7 **(a)**).

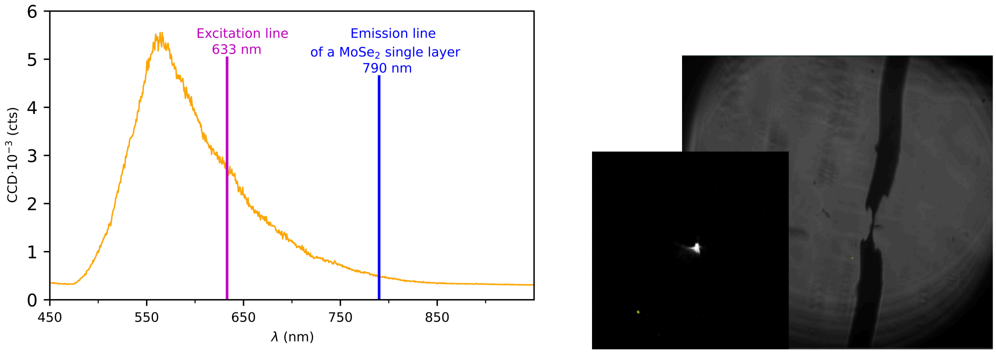

(a)

(b)

Figure 7: Characterization of plasmonic emission at the Ag tip- Ag(111) surface nanocavity. **(a)** Emission spectrum of the nanocavity. Broad plasmonic resonance with maxima in the red region. Pink and blue vertical lines depict the wavelength of the excitation laser used in this experiment, and the expected emission line of the material to be studied, a single layer $MoSe_2$. **(b)** STM junction. The bright point is the light emitted by the plasmon of the tip. Parameters: Voltage 2.6 V, Current 1nA.

3.2.2 Near-Field coupling

Photon coupling to the nanocavity was tested by measuring field emission resonances (FERs) by STS. For this, a 633 nm ($h\nu = 1.96$ eV) laser beam, approximately 50 μm in diameter, was precisely focused on the tip-sample nanocavity. Efficient coupling leads to a reduction of the resonance energies due to the inelastic electron-plasmon interaction (Figure 8 (**a**)).

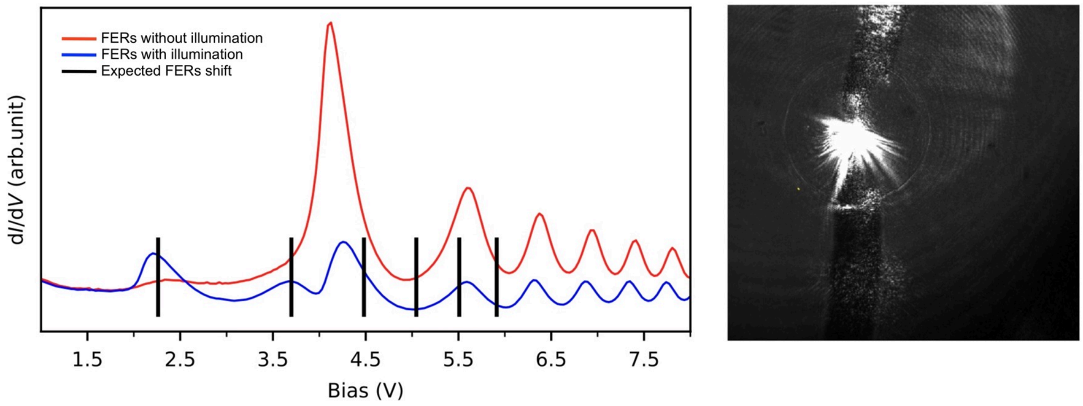

(a) (b)

Figure 8: Coupling of the laser with the STM junction. (**a**) FER, measured as dI/dV at constant current feedback with an Ag tip covered by Au on a clean Ag(111) surface sample with (blue line) and without (red line) the illumination source. Vertical black lines indicate the expected position of the peaks in for a 100% efficient conversion. (**b**) STM junction. Current set-point: 200pA, Lock-in modulation amplitude: 50mV.

At bias voltages close to and above the work function, tip electrons are emitted as FERs, that is in the Fowler–Nordheim tunneling regime[4], and can populate image potential states (IPS)[5] of the sample surface. Without laser illumination, FER peaks appear (Figure 9 (**a**)) when the bias voltage matches the respective resonances, *i.e.*, electrons at the Fermi level of the tip tunnel into the IPS. Under illumination (Figure 9 (**b**)), efficient coupling induces energy transfer from the excited EM modes within the nanocavity (laser) to the tunneling electrons, which is translated into a downshift of the FER due to plasmon-assisted tunneling.

This phenomenon is observed in Figure 8 (**a**), since the shift related to the first FER of Ag(111), 1.89 eV, almost coincides with the incident photon energy, 1.96 eV, indicating a discrepancy of 3.57%. In most practical cases, the conversion does not need to be entirely efficient. This is denoted by the fact that the spectra reflect a convolution of the set of peaks corresponding to the plasmon-assisted and intrinsic resonances. The expected positions of the FERs under illumination for a 100% efficient conversion are indicated by vertical black lines in Figure 8 (**a**). These were obtained by subtracting the excitation photon energy from the FER peaks positions observed without illumination, measured by fitting the experimental data using a Gaussian-Lorentzian convolution (Appendix B, Figure

---

[4] The Fowler–Nordheim tunneling regime [SC94] describes electrons tunneling through a potential barrier under the influence of an extremely intense electric field.

[5] Quantized electronics states bound to a metal surface with band gap near the vacuum level. The Coulomb-like attractive image force, experienced by any charged particle in front of a conductive material, and the repulsive response of the substrate form a potential well which traps weakly bound electrons.

21 **(a)**). In addition, the third blue peak at 4.3 eV is noticeably shifted to the left from the expected position at 4.5 eV and exhibits asymmetry. This results from the overlapping contributions of the third FER under illumination (converted electrons) and the residual first FER peak without illumination (non-converted electrons). Comparing the intensity of the first FER under illumination to that of this third one, which predominantly represents the first FER without illumination, suggests that the efficiency of the conversion process is approximately 50%.

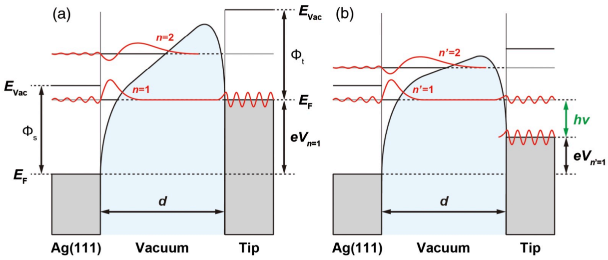

Figure 9: Energy diagram scheme of the Au tip-vacuum-Ag(111) junction (a) without and (b) with laser excitation (energy $h\nu$). Electron wave functions are depicted along with FERs. The schematic potential in the junction is represented with the blue shaded area. Image taken from [LWK18].

Table 2: Parameters notation

Symbol	Description
E_F	Fermi level
E_{vac}	Vacuum level
V_s	Sample bias
d	Gap distance
n, n'	Index of the FER
$\phi_{s/t}$	Work function of the sample/tip
$V_{n,n'}$	FER voltage without/with laser
$h\nu$	Incident photon energy

4 Results

The heterostructure chosen to investigate excitons behaviour in nanostructure 2D materials comprises $MoSe_2$ monolayer or thin multi-layer on NPG nanoribbons on an Au substrate. This sample was prepared at ICN2 laboratories and subsequently measured by PSTM at facilities in Prague. Specifically, the experiment was conducted in an UHV chamber equipped with a LT-STM and an optical setup described in Figure 10. All measurements were performed at around 5 K using an Au-coated Ag tip and the sample was never exposed to air throughout the entire preparation. Beyond studying the excitons' nature and behaviour, it would be of great interest to confine them in specific controlled regions for device applications, particularly in the creation of interacting single quantum emitters. The experiment hypothesis is that the periodic electronic structure of the underlying NPG induces a periodic potential in the adjacent layers of $MoSe_2$, potentially confining excitons in specific regions.

All PSTM techniques require the integration of an optical setup to introduce or extract light from the junction. In the optical setup (Figure 10) used for this experiment, the excitation source was a 633 nm HeNe continuous-wave laser focused on the STM junction using a parabolic mirror mounted on a commercial Createc 4.7 K STM working under UHV conditions. The incident beam, collimated with a 15 mm focal length lens, was polarized along the tip-sample axis, with a total power set at 0.5 mW. Within the STM nanocavity, there was a lense at a fixed position to the tip, with its focus positioned at the apex to direct the amplified signal to the detectors outside the STM chamber. The emitted light from the junction was collected by a mirror and filtered using a 633 nm bandpass edge filter. TERS and TEPL spectra were measured in cumulative mode by an Andor Kymera 328i spectrograph equipped with four different gratings (150 l/mm, 300 l/mm, 600 l/mm and 1200 l/mm) connected to a custom control computer.[dCFSD+24]

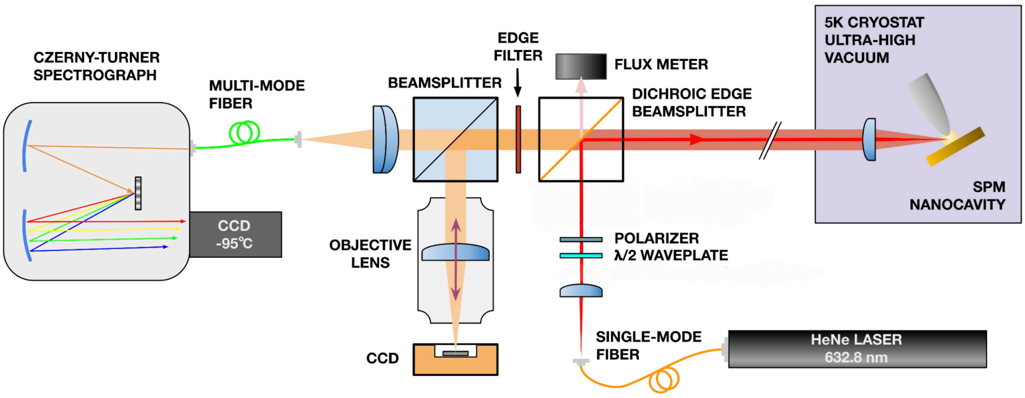

Figure 10: Scheme of the optical setup for TERS and TEPL measurements at 5 K and cryogenic conditions. Image taken from [dCFSD+24].

4.1 Sample preparation: $MoSe_2$/NPG heterostructure.

In condensed matter, electrons and holes can recombine to form quasiparticles known as excitons, emitting a photon (for a radiative decay) with an energy corresponding to the sum of electron and hole energies, reduced by the exciton binding energy. Excitons are central to understanding light absorption, emission, and energy transfer in solids. The mean distance between charge carriers in a material is determined by the Coulomb interaction and is strongly influenced by the dielectric constant and the charge mobility. Excitons can diffuse from their place of creation via nonradiative energy transfer processes and become localized in exciton traps within crystals. These traps may arise from chemical impurities, structural disorder, or punctual defects. In addition, the excitonic properties of materials change when structure sizes are reduced to the nanometer scale. Recent research [BHR13] has focused on excitons in 2D systems of transition-metal dichalcogenides (TMDs), whose optical response is well understood in terms of neutral and charged excitons. However, optical characterization of these materials at the nanoscale poses a challenge that only PSTM can circumvent.

TMDs have attracted significant interest due to their unique electronic, optical and optoelectronic properties in the monolayer (ML) and few-layer forms, which differ from their bulk counterparts. These properties make them promising candidates for the fabrication of optoelectronic devices and integrated electronic circuits. Specifically, $MoSe_2$ constitutes a TMD material ideally suited for exploring exciton dynamics [SKM+16, KGMK17a]. Its low dielectric constant results in a strong Coulomb interaction between electrons and holes, leading to more localized, tightly bound excitons with binding energies around 186 meV [HRC+18]. Its optimal band alignment ensures that the excitonic energy lies within the NPG/Au gap, minimizing the probability of excitons tunneling into NPG (quenching light emission) and thereby favouring radiative decay. Additionally, its large excitonic energy and small excitonic radius (around 1.1 nm in ML $MoSe_2$ [LvBL+21]), which are comparable to the pore sizes of NPG, make it ideal for confinement. Spatial confinement of excitons within the plane increases their interaction time with light, possibly causing brighter and more efficient light-emitting devices. Moreover, it can modify the energy levels and properties of excitons, allowing for precise control over the wavelengths of light emission.

On the other hand, NPG is a unique semiconducting graphene nanoarchitecture with a bandgap induced by the spacing between the pores [MdCVV+23]. It exhibits filtering and sensing functionality, strongly dependent on the size and shape of the pores. In addition, its distinct topology provides one-dimensional anisotropy and different types of localization in the electronic states. The primary interest of choosing this semiconductor lies in its periodic, atomically-precise potential, which can be modulated by tailoring the pores' size [MVVS+18]. The NPG may imprint its intrinsic well potential to the TMD, potentially confining the excitons within these wells.

4.1.1 Synthesis and *in-situ* characterization of NPG

NPG with atomic precision was synthesized via a series of thermally controlled on-surface reactions on an Au substrate under UHV conditions [MVVS+18]. This approach employs a specifically designed monomer precursor (DP-DBBA) to achieve selective inter-ribbon connections, resulting in a NPG structure with both semiconducting and nanosieving functionalities. It also enables the formation of graphene nanoribbons (GNR) with precisely defined pore sizes and a highly ordered arrangement. For this experiment, the periodicity of NPG is 0.8 and 1.6 nm in the short and long directions (Figure 11), so the pore size matches the exciton size dimensions of $MoSe_2$. Moreover, when performing the TEPL/STML measurements on the sample, emission peaks related to the optical response of the NPG will likely be observed. Therefore, a Raman/PL study of the NPG was also conducted as a reference for the experiment's development (Figure 12).

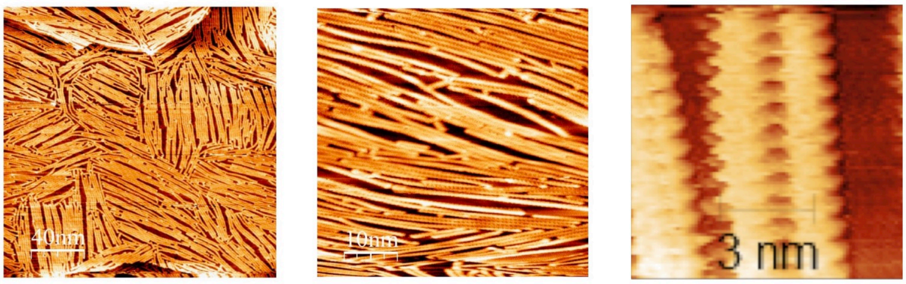

Figure 11: STM images taken at ICN2 during NPG synthesis. Lattice structure of GNR on Au(111) substrate before depositing the $MoSe_2$.

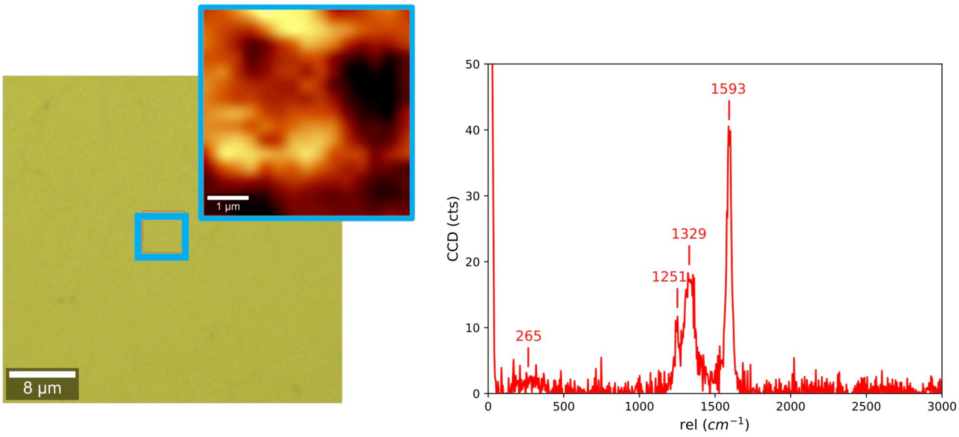

(a)

(b)

Figure 12: Spectra measured at different positions on NPG on Au. **(a)** Exact position where the spectra were measured. **(b)** Raman spectra. Grating 1800l/mm.

4.1.2 Transfer and characterization of $MoSe_2$ on NPG.

NPG on Au was transferred via a UHV suitcase to an Ar-filled glove box where thin $MoSe_2$ flakes were deposited on top via mechanical exfoliation (Appendix D.2 Figure 31). This method involves separating layers of different thicknesses from the layered bulk crystal and placing them onto a substrate using a viscoelastic Polydimethylsiloxane (PDMS) stamp (see Appendix D.2, Figure 31) [KGMK17b].

Once prepared, the $MoSe_2$/NPG/Au sample was transferred to an Ar-filled cell used for optical microscopy, Raman and PL measurements. Optical microscopy was employed to locate $MoSe_2$ flakes on NPG (Figure 13), highlighting the presence of some few-layer $MoSe_2$/NPG regions, including possible small areas of ML $MoSe_2$. To determine the thickness of the $MoSe_2$ flakes and assess their optical response, PL and Raman measurements were performed, as shown in Figure 14. By comparing the obtained spectra with tabulated emission values from literature [TSB^+13a] for $MoSe_2$, regions exhibiting 1, 2 and 3 optically active ML were identified.

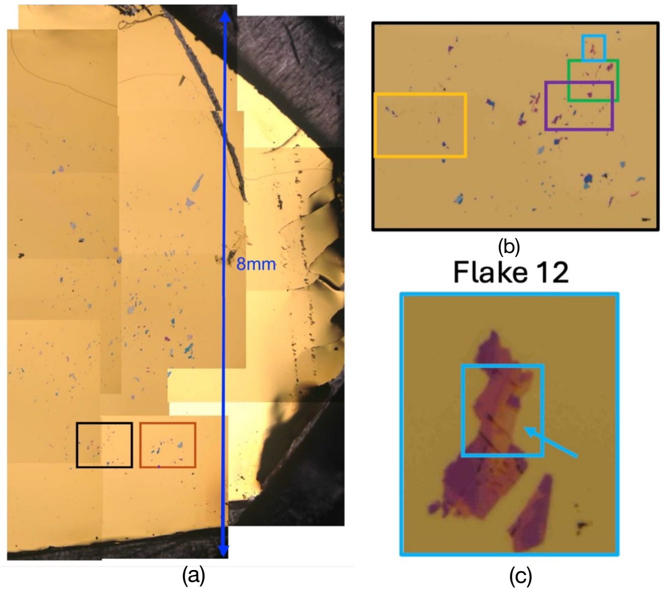

Figure 13: $MoSe_2$ flakes transferred onto NPG/Au. **(a)** Overall image of the $MoSe_2$/NPG/Au sample. **(b)** Region showing multiple flakes, with highlighted areas containing few-layer $MoSe_2$, as observed via optical microscopy. **(c)** Flake 12, with a possible monolayer region indicated by a blue arrow.

However, in certain regions, the Raman spectra did not align well with the expectations from optical spectroscopy. This inconsistency can be attributed to the inherent heterogeneity of exfoliated few-layer flakes of $MoSe_2$, resulting in spatial variability at the nanoscale in their Raman and PL spectra. Therefore, PSTM is essential for unambiguously characterizing the number of $MoSe_2$ layers.

Note: These two previous sections were entirely carried out by the team specialized in the synthesis and transfer of samples at ICN2. However, for completeness, it is appropriate to include them in this thesis and proceed with the analysis of the data provided during the synthesis/transfer process.

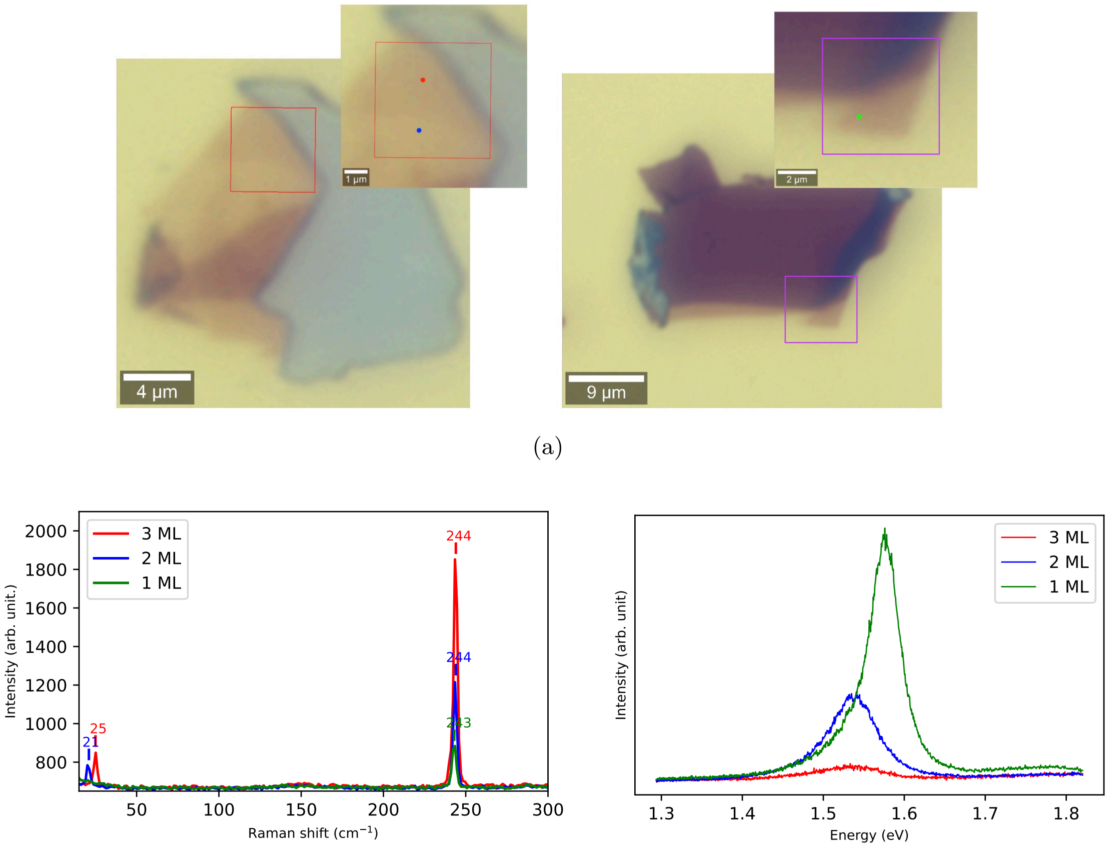

(a)

(b)

(c)

Figure 14: Spectra measured at different positions on few-layer MoS_2 on NPG. **(a)** Exact positions where the spectra were measured. **(b)** Raman spectra for 1,2 and 3 ML of $MoSe_2$. Grating 1800l/mm. **(c)** PL spectra for 1,2 and 3 ML of $MoSe_2$. Grating 300l/mm.

4.1.3 Transport to Prague and *in-situ* UHV annealing preparation

The sample was transported under Ar atmosphere to a glove box and then transferred into a static-UHV suitcase for shipping to Prague. Upon arrival, it was introduced into the UHV chamber of the PSTM, and subjected to an annealing process (3 hours at 250°) to remove adsorbed contaminants. Although the sample was shielded from direct air exposure, it might have seen air briefly due to the lack of coupling system between the UHV boxes and the STM chamber. In this context, annealing involves a heat treatment that alters the physical and sometimes chemical properties of a material, cleaning the surface by causing adsorbates to evaporate at elevated temperatures. The temperature range of 250-300° is commonly used for outgassing procedures in UHV chambers to desorb weakly bound molecules like water vapor and other impurities without damaging the sample's structure. Recent studies [PZCRdC$^+$24] show that NPG can withstand temperatures above 500° in UHV conditions, while $MoSe_2$ can maintain its structural integrity up to 400° on graphene substrates [BBE$^+$23].

4.2 Characterization of the MoSe2/NPG heterostructure by Photon-STM.

The interest in identifying ML regions of $MoSe_2$ is two-fold. First, $MoSe_2$ exhibits a transition from an indirect bandgap semiconductor in the bulk to a direct bandgap semiconductor in the monolayer and few-layer limit (bandgap value around 1.56 eV [HRC$^+$18]). Due to strong Coulomb interaction in these single-layer regions, the optical properties are dominated by excitons. Second, understanding the spatial distribution of ML domains is essential for testing the hypothesis of exciton confinement. Layers closer to the NPG substrate are expected to sense more intensely the NPG periodic well potential, facilitating exciton confinement.

Once the sample is introduced in the STM chamber, the first step entails selecting an area with potential ML flakes large enough to land and scan under stable conditions. Flake 12 was chosen as the most suitable for measuring (Figure 15) because it was easy to identify during scanning, relatively large and contained few-layer regions according to Raman/PL. Nevertheless, the region of flake 12 which might be a ML is too small to selectively land on, requiring to scan the area in search of thinner, atomically clean and smooth TMD terraces.

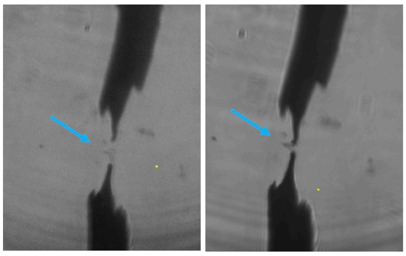

Figure 15: View through the LT-STM lens in the approach. The image is vertically flipped with respect to the optical microscope at ICN2 (Figure 13).

4.2.1 Topographic and electronic characterization.

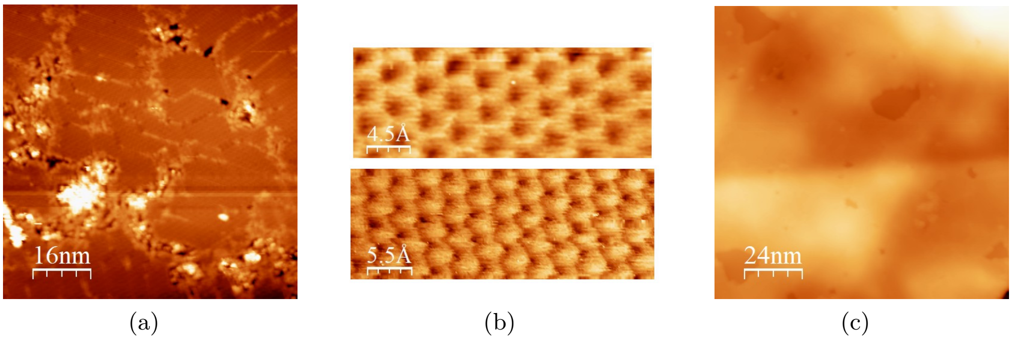

(a)

(b)

(c)

Figure 16: STM topographic images of flake 12: $MoSe_2$ on NPG on Au(111) after 3 hours of annealing at 250°. **(a)** $MoSe_2$ terrace displaying twin boundaries and 3D-like contaminants (likely of PDMS-origin). **(b)** Lattice structure of the TMD with atomic resolution. The contrast-inversion between the two images is due to changes at the tip apex. **(c)** $MoSe_2$ clean region showing surface undulations/bubbles. Zoom images in Appendix D.2.

Flake 12 was remarkably clean and easy to scan, allowing observation of the honeycomb lattice of $MoSe_2$ (Figure 16 **(b)**). The measured lattice parameter with STM is 3.4 Å, whereas the tabulated value is 3.32 Å. This indicates a discrepancy of 2.4%, which can be partially attributed to strain from the interaction with NPG. On the other hand, as shown in Figure 16 **(c)**, there are bubbles on the TMD sub-surface that may act as exciton recombination centres due to the reduced bandgap from the local strain [GV$^+$23]. These undulations are primarily attributed to the incidental contamination present on individual layers before the deposition of the TMD on the substrate. The forces binding adjacent layers facilitate the coalescence of trapped matter into minute bubbles, creating larger inter-bubble areas that are sharp and free of contamination through a process known as self-cleaning [GV$^+$23]. Recent studies have indicated that the presence of bubbles leads to variations in the local properties of 2D materials, serving as quantum-dot emitters because of the interplay between the strain-induced confinement and changes in the local dielectric environment. They appear as bright protrusions, predominantly found at the step edges of the sample. No Moiré pattern[6] is observed, confirming the decoupling of $MoSe_2$ from the Au substrate over these undulated regions. In addition, a minority area of $MoSe_2$ (Figure 16 **(a)**) exhibits twin boundaries[7] [BWL+16].

The topography of the NPG/Au/mica was also characterized to verify the quality of the sample. As shown in Figure 17 **(a)** and **(b)**, stark changes in the morphology of exposed GNR after annealing denote structural degradation compared to when it was synthesized (Figure 11). Various causes were considered, such as contamination during transport, but they were quickly dismissed due to the good condition of a sample with only NPG on Au (no TMD). In this reference sample (Figure 18), the NPG atomic lattice remained unchanged, with only surface adsorbates resulting from a few minutes of air exposure before introducing it in the UHV chamber. Consequently, the most probable option of NPG degradation is its interaction with residual PDMS during UHV annealing.

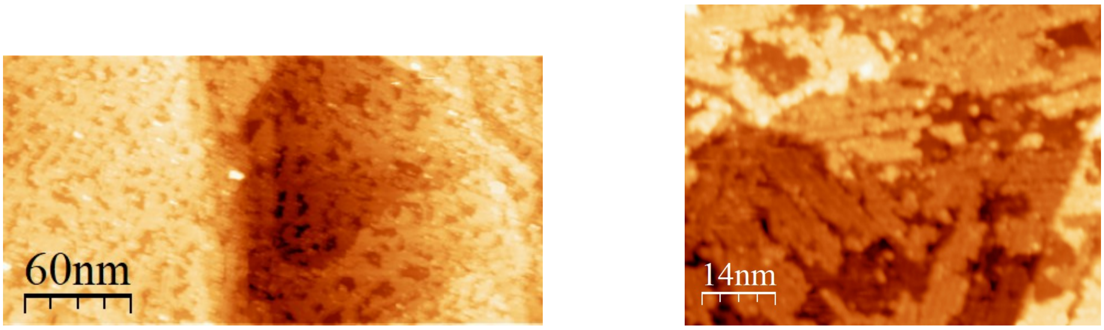

(a) (b)

Figure 17: STM images showing the NPG on Au(111) lattice structure for the sample to be used in the experiment.**(a)** and **(b)** Degraded GNR of the sample TMD/NPG/Au after 3 hours of annealing at 250°.

After cleaning the sample, the primary objective was to identify a potential monolayer large enough for stable scanning. A promising clean region at the TMD-NPG interface was located (Figure 19**(a)**), where different layers of the $MoSe_2$ were distinctly visible. The sample contains coexistent regions of monolayer (ML), bilayer (BL), and trilayer (TL) $MoSe_2$. Variations in the electronic structure of the TMD are experimentally observed using STS [LBB+15] to characterize the number of layers. The dI/dV spectra shown in Figure 19 **(b)** reveal a relatively wide bandgap, around 2 eV and 1.6 eV for bottom/top positions respectively, with features in both the valence and conduction band regions. The resulting bandgap values depend on the layer thickness, and by comparing them with the values obtained in previous experiments (1.56 eV BL and 2.18 eV TL) [KVS+10, BUdJ+15], it appears that the border corresponds to a transition 2-3 ML.

---

[6] On Au(111) the monolayer $MoSe_2$ flakes exhibit a lattice mismatch with the underlying surface, forming a moiré superstructure.[KLF18]

[7] Specific type of grain boundary that separates two domains with mirror-symmetric crystal lattices. These boundaries were most probably introduced in the exfoliated flakes during the electrochemical exfoliation process.[YWZ+20]

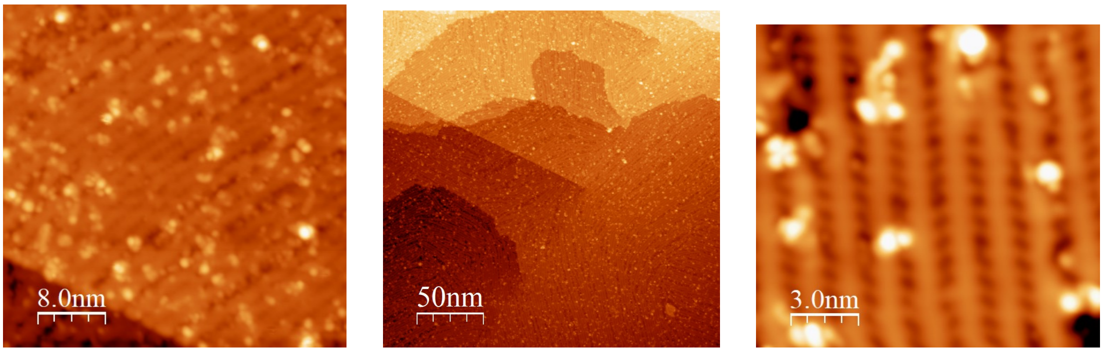

(a) (b) (c)

Figure 18: STM images of NPG on Au(111) for a reference sample with no TMD transfered on top. The sample was exposed to air for a few minutes before annealing (250° for 3 hours). The bright granular points are adsorbates accumulated on the surface, but the nanoribbons conserve the lattice structure with no apparent degradation. **(a)** Border NPG-Au. **(b)** NPG deposited on Au, revealing distinct Au steps in clear view. **(c)** GNR.

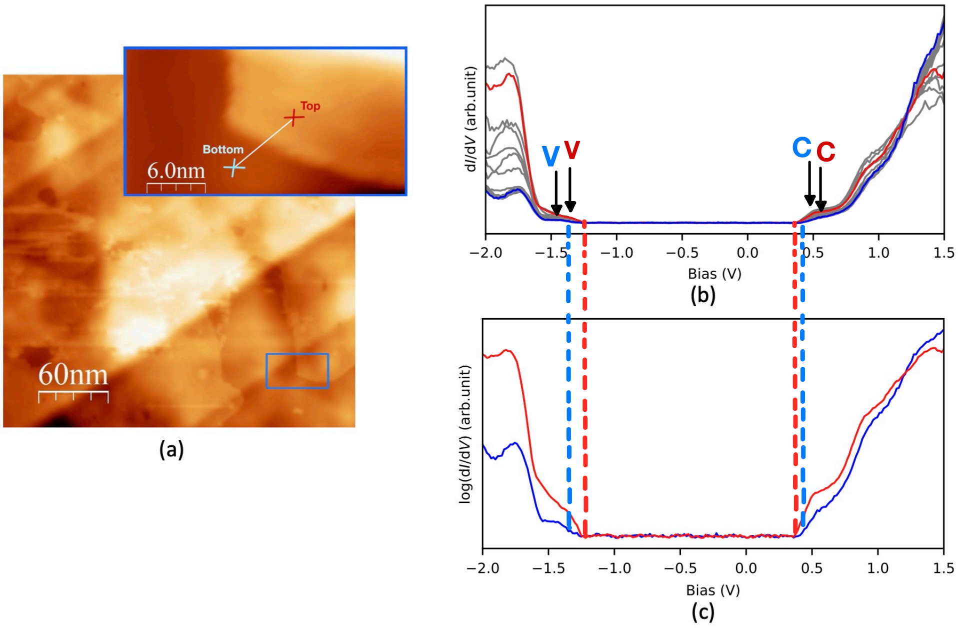

(a) (b) (c)

Figure 19: dI/dV spectra taken by STS at different positions on few-layer $\mathrm{MoSe_2}$ on NPG.**(a)** Exact positions where the spectra were measured. **(b)** Line spectra measured across a single-layer $\mathrm{MoSe_2}$ step (depicted by the white line), showing the progressive change in the bandgap. **(c)** Same STS curves shown on a logarithmic scale to highlight the electronic band edges (marked by dashed lines). Prominent features that determine the band edges (V,C) are also depicted.

4.2.2 Optical characterization.

No sign of excitation-emission from the NPG-supported $\mathrm{MoSe_2}$ was detected. This is shown in the TERS and PL spectra measured using 633-nm laser excitation, at incremental tip-surface distances (Figure 20). The initial observation that NF and FF spectra coincide implies no amplification in the nanocavity, but this does not necessarily indicate a lack of luminescence in the FF. However, previous measurements predict the presence of emission peaks from the excitation of both NPG (Figure 12 **(b)**) and TMD (Figure 14 **(b)** and **(c)**), which are not present in this experiment, indicating no luminescence detected in the sample.

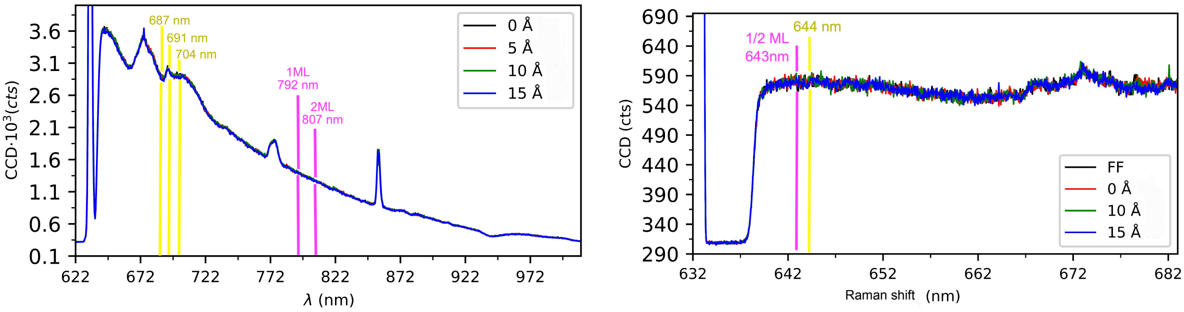

(a) (b)

Figure 20: Spectra measured with a 633nm HeNe laser in flake 12 at different tip-sample distances relative to a reference point. **(a)** PL spectra. Grating 1: 150 l/mm. **(b)** Raman spectra. Grating 4: 600 l/mm. Tabulated emission lines of 1-2 ML $MoSe_2$ (pink lines, see reference [TSB+13b]) and NPG (yellow lines, corresponding to the emission lines from Figure 12) are depicted. Stabilization conditions: Current 43 pA, Voltage 1.7 V.

The lack of luminescence may be attributed to several factors mostly related to the sample's condition (*e.g.*, contamination) and its optical response. However, these options were quickly discarded since characteristic PL and Raman features were measured at ICN2 before and after the TEPL experiment, indicating the sample was optically active during the measurements. The potential loss of amplification in the nanocavity was also considered but refuted, as the tip remained plasmonically active throughout the process. Furthermore, the good laser alignment was repeatedly verified by observing the electron-induced plasmon (Figure 7 **(b)**). Although the laser's power density ($0.5\ \mu W/\mu m^2$) was considerably lower than that used in other experiments ($30\ \mu W/\mu m^2$) [TSB+13b], this does not entirely justify the complete absence of excitonic emission. Therefore, the lack of luminescence is most likely due to the weak PL signal of the measured multilayer (Appendix D.2 Figure 32 **(g)**).

4.3 Research Summary

This study showcases highly controlled navigation and landing on wide $MoSe_2$ flakes. Atomically clean and smooth few-layer $MoSe_2$ regions were successfully identified on NPG, with non-covered GNR exhibiting degradation due to residual PDMS. Although estimation of layer numbers was enabled by STS, single-layer regions proved too small and scarce for selective landing. The absence of detectable NF luminescence is attributed to the weak PL signal emitted by the measured few-layer $MoSe_2$.

5 Conclusions and outlook

This thesis provides a comprehensive overview of Photon-STM techniques for studying 2D heterostructures, elucidating both the theoretical principles and the experimental methodologies employed. It highlights the preparation and realization of an experiment focused on exploring exciton superlattice behaviour at the ML $MoSe_2$/NPG interface with sub-nm spatial resolution, combining PL and TERS spectroscopy within an STM nanocavity.

$MoSe_2$ flakes exhibit atomically clean and flat regions, allowing for atomic resolution scanning. PL spectroscopy was conducted in an apparent thin region, but no tip-enhanced optical response was obtained. The primary obstacle encountered was the difficulty of locating sufficiently large $MoSe_2$ monolayer areas for effective measurement. Therefore, future experiments will prioritize achieving larger few-layer flakes. Even if the ambitious initial objective of spatially confining excitations was not achieved, these endeavors have laid the groundwork for refining experimental techniques and enhancing sample preparation methodologies.

The improvement plan also involves a new PDMS-free transfer method for depositing TMDs on NPG. Eliminating PDMS from the mechanical exfoliation process is expected to reduce residual contamination and prevent the degradation of NPG nanoribbons during annealing. For that purpose, NPG will be grown on masked Au on mica samples. Masked Au, in this context, refers to a technique where part of the Au surface is covered during the deposition to provide large, clean Au areas for *in-situ* tip preparations. By ensuring better quality and stability of the sample surface, this approach is intended to improve the precision and reliability of the measurements.

In conclusion, this thesis explores the potential of PSTM for studying exciton behaviour in $MoSe_2$. In particular, their engineering by imprinting superlattice potentials through interfacing with nanostructures such as NPG. While challenges with the sample limited the ability to achieve spatial confinement of excitons, the obtained results leave a very promising path for a successful future experiment. These findings underscore the need for several adjustments, particularly in sample preparation, to thoroughly investigate exciton engineering in 2D heterostructures. This work also proposes a new approach for future research, promoting its continuation for the sake of the completeness of the study.

Bibliography

[BBE+23] Lars Buß, Nicolas Braud, Moritz Ewert, Matteo Jugovac, Tevfik Onur Menteş, Andrea Locatelli, Jens Falta, and Jan Ingo Flege. Unraveling van der Waals epitaxy: A real-time *in-situ* study of $MoSe_2$ growth on graphene/Ru(0001). *Ultramicroscopy*, 250:113749, May 2023.

[BHR13] Timothy C. Berkelbach, Mark S. Hybertsen, and David R. Reichman. Theory of neutral and charged excitons in monolayer transition metal dichalcogenides. *Phys. Rev. B*, 88:045318, Jul 2013.

[BUdJ+15] Aaron J. Bradley, Miguel M. Ugeda, Felipe H. da Jornada, Diana Y. Qiu, Wei Ruan, Yi Zhang, Sebastian Wickenburg, Alexander Riss, Jiong Lu, Sung-Kwan Mo, Zahid Hussain, Zhi-Xun Shen, Steven G. Louie, and Michael F. Crommie. Probing the role of interlayer coupling and coulomb interactions on electronic structure in few-layer $MoSe_2$ nanostructures. *ACS Nano*, 15:2594–2599, Mar 2015.

[BWL+16] Sara Barja, Sebastian Wickenburg, Zhen-Fei Liu, Yi Zhang, Hyejin Ryu, Miguel M. Ugeda, Zahid Hussain, Zhi-Xun Shen, Sung-Kwan Mo, Ed Wong, Miquel B. Salmeron, Feng Wang, Michael F. Crommie, D. Frank Ogletree, Jeffrey B. Neaton, and Alexander Weber-Bargioni. Charge density wave order in 1D mirror twin boundaries of single-layer $MoSe_2$. *Nature Physics*, 12:751–756, Apr 2016.

[Che07] C. Julian Chen. *Introduction to Scanning Tunneling Microscopy.* Oxford University Press, July 2007.

[CS22] Yi Cao and Mengtao Sun. Tip-enhanced Raman spectroscopy. *Reviews in Physics*, 8:100067, Jun 2022.

[dCFSD$^+$24] Rodrigo Cezar de Campos Ferreira, Amandeep Sagwal, Jiří Doležal, Sofia Canola, Pablo Merino, Tomáš Neuman, and Martin Švec. Supporting information for resonant Tip-Enhanced Raman Spectroscopy of a single-molecule Kondo system. *ACS Nano*, 18:13164–13170, May 2024.

[DCMv21a] Jiří Doležal, Sofia Canola, Pablo Merino, and Martin Švec. Exciton-trion conversion dynamics in a single molecule. *ACS Nano*, 15:7694–7699, Apr 2021.

[DCMv21b] Jiří Doležal, Sofia Canola, Pablo Merino, and Martin Švec. Nanoscale mapping of excitonic processes in single-layer MoS_2 using Tip-nhanced Photoluminescence Microscopy. *ACS Nano*, 15:7694–7699, Apr 2021.

[DMN$^+$20] Jiří Doležal, Pingo Mutombo, Dana Nachtigallová, Pavel Jelínek, Pablo Merino, and Martin Švec. Mechano-optical switching of a single molecule with doublet emission. *ACS Nano*, 14:8931–8938, Jun 2020.

[DVK$^+$10] Jens Dorfmüller, Ralf Vogelgesang, Worawut Khunsin, Carsten Rockstuhl, Christoph Etrich, and Klaus Kern. Plasmonic nanowire antennas: Experiment, simulation, and theory. *Nano Letters*, 10:3596–3603, Aug 2010.

[Fey60] R. P. Feynman. There's plenty of room at the bottom. *Caltech Engineering and Science*, 23:22–26, 1960.

[FHM74] M. Fleischmann, P.J. Hendra, and A.J. McQuillan. Raman spectra of pyridine adsorbed at a silver electrode. *Chemical Physics Letters*, 26:163–166, May 1974.

[FIB16] Large volume serial section tomography by Xe Plasma FIB dual beam microscopy. *Ultramicroscopy*, 161:119–129, 2016.

[FNMG$^+$17] Riccardo Frisenda, Efrén Navarro-Moratalla, Patricia Gant, David Pérez De Lara, Pablo Jarillo-Herrero, Roman V. Gorbachev, and Andres Castellanos-Gomez. Recent progress in the assembly of nanodevices and van der Waals heterostructures by deterministic placement of 2D materials. *Chemical Society Reviews*, 47, Aug 2017.

[GGA$^+$21] Rico Gutzler, Manish Garg, Christian R. Ast, Klaus Kuhnke, and Klaus Kern. Light–matter interaction at atomic scales. *Nature Reviews Physics*, 3:441–453, Jun 2021.

[GMR$^+$17] Christoph Große, Pablo Merino, Anna Rosławska, Olle Gunnarsson, Klaus Kuhnke, and Klaus Kern. Submolecular electroluminescence mapping of organic semiconductors. *ACS Nano*, 11:1230–1237, Jan 2017.

[GRCS88] J.K. Gimzewski, B. Reihl, J.H. Coombs, and R.R. Schlittler. Photon emission with the scanning tunneling microscope. *Z. Physik B - Condensed Matter*, 72:497–501, Apr 1988.

[GV$^+$23] Michele Gastaldo, Javier Varillas, Álvaro Rodríguez, Matej Velický, Otakar Frank, and Martin Kalbác. Tunable strain and bandgap in subcritical-sized MoS_2 nanobubbles. *2D Materials and Applications*, 7, Oct 2023.

[GW93] H.-J. Guntherodt and R. Wiesendanger. *Scanning Tunneling Microscopy I*. Springer-Verlag, August 1993.

[HLC$^+$11] Naomi J. Halas, Surbhi Lal, Wei-Shun Chang, Stephan Link, and Peter Nordlander. Plasmons in strongly coupled metallic nanostructures. *Chemical Reviews*, 111:3913–3961, May 2011.

[HRC$^+$18] B. Han, C. Robert, E. Courtade, M. Manca, S. Shree, T. Amand, P. Renucci, T. Taniguchi, K. Watanabe, X. Marie, L. E. Golub, M. M.

Glazov, and B. Urbaszek. Exciton states in monolayer $MoSe_2$ and $MoTe_2$ probed by upconversion spectroscopy. *Phys. Rev. B*, 8:031073, Sep 2018.

[IMII+17] Hiroshi Imada, Kuniyuki Miwa, Miyabi Imai-Imada, Shota Kawahara, Kensuke Kimura, and Yousoo Kim. Single-molecule investigation of energy dynamics in a coupled plasmon-exciton system. *Phys. Rev. Lett.*, 119:013901, Jul 2017.

[JBLF18] Varun Jain, Mark C. Biesinger, Matthew R. Linford, and J. Franke. The gaussian-lorentzian sum, product, and convolution (voigt) functions in the context of peak fitting X-ray photoelectron spectroscopy (XPS) narrow scans. *Applied Surface Science*, 447:548–553, Mar 2018.

[JHZ+19] Robin R. Jones, David C. Hooper, Liwu Zhang, Daniel Wolverson, and Ventsislav K. Valev. Raman techniques: Fundamentals and frontiers. *Nanoscale Res Lett.*, 14:231, Jul 2019.

[JNB+23] Song Jiang, Tomáš Neuman, Alex Boeglin, Fabrice Scheurer, and Guillaume Schull. Topologically localized excitons in single graphene nanoribbons. *Science*, 379:1049–1054, Mar 2023.

[KGMK17a] Klaus Kuhnke, Christoph Große, Pablo Merino, and Klaus Kern. Atomic-scale imaging and spectroscopy of electroluminescence at molecular interfaces. *Chemical Reviews*, 117:5174–5222, Mar 2017.

[KGMK17b] Klaus Kuhnke, Christoph Große, Pablo Merino, and Klaus Kern. Atomic-scale imaging and spectroscopy of electroluminescence at molecular interfaces. *Chemical Reviews*, 117:5174–5222, Mar 2017.

[KLF18] Nils Krane, Christian Lotze, and Katharina J. Franke. Moiré structure of MoS_2 on Au(111): Local structural and electronic properties. *Surface Science*, 39:136–142, Mar 2018.

[KMI+19] Kensuke Kimura, Kuniyuki Miwa, Hiroshi Imada, Miyabi Imai-Imada, Shota Kawahara, Jun Takeya, Maki Kawai, Michael Galperin, and Yousoo Kim. Selective triplet exciton formation in a single molecule. *Nature*, 570:210–213, Jun 2019.

[KSB+16] Sergei V. Kalinin, Evgheni Strelcov, Alex Belianinov, Suhas Somnath, Rama K. Vasudevan, Eric J. Lingerfelt, Richard K. Archibald, Chaomei Chen, Roger Proksch, Nouamane Laanait, and Stephen Jesse. Big, deep, and smart data in scanning probe microscopy. *ACS Nano*, 10:9068–9086, Sep 2016.

[KSS+15] Alexander E. Krasnok, Alexey P. Slobozhanyuk, Constantin R. Simovski, Sergei A. Tretyakov, Alexander N. Poddubny, Andrey E. Miroshnichenko, Yuri S. Kivshar, and Pavel A. Belov. An antenna model for the Purcell effect. *Scientific Reports*, 5:12956, Aug 2015.

[KVS+10] Antal A. Koós, Péter Vancsó, Márton Szendrő, Gergely Dobrik, David Antognini Silva, Zakhar I. Popov, Pavel B. Sorokin, Luc Henrard, Chanyong Hwang, László P. Biró, and Levente Tapasztó. Influence of native defects on the electronic and magnetic properties of CVD grown $MoSe_2$ single layers. *ACS Nano*, Nov 2010.

[LBB+15] Xiaolong Liu, Itamar Balla, Hadallia Bergeron, Gavin P. Campbell, Michael J. Bedzyk, and Mark C. Hersam. Rotationally commensurate growth of mos_2 on epitaxial graphene. *ACS Nano*, 10:1067–1075, Nov 2015.

[LLK+20] Hyeongwoo Lee, Dong Yun Lee, Min Gu Kang, Yeonjeong Koo, Taehyun Kim, and Kyoung-Duck Park. Tip-enhanced photoluminescence nano-spectroscopy and nano-imaging. *Nanophotonics*, 9:3089–3110, Feb 2020.

[Loc23] *Principles of lock-in detection and the state of the art.* Technische Universität München, Garching, Germany, Apr 2023.

[LRS$^+$23] Luis E. Parra López, Anna Rosławska, Fabrice Scheurer, Stéphane Berciaud, and Guillaume Schull. Tip-induced excitonic luminescence nanoscopy of an atomically resolved van der Waals heterostructure. *Nature Materials*, 22:482–488, Apr 2023.

[Luc04] Anne-Sophie Lucier. Preparation and characterization of tungsten tips suitable for molecular electronics studies. Master thesis, McGill University, Quebec, Canada, Apr 2004.

[LvBL$^+$21] Erfu Liu, Jeremiah van Baren, Zhengguang Lu, Takashi Taniguchi, Kenji Watanabe, Dmitry Smirnov, Yia-Chung Chang, and Chun Hung Lui. Exciton-polaron rydberg states in monolayer $MoSe_2$ and wse_2. *Nat Communications*, 12:6131, Sep 2021.

[LWK18] Shuyi Liu, Martin Wolf, and Takashi Kumagai. Plasmon-assisted resonant electron tunneling in a scanning tunneling microscope junction. *Physical Review Letters*, 121:1–6, Nov 2018.

[MdCVV$^+$23] César Moreno, Xabier Diaz de Cerio, Manuel Vilas-Varela, Maria Tenorio, Ane Sarasola, Mads Brandbyge, Diego Peña, Aran Garcia-Lekue, and Aitor Mugarza. Molecular bridge engineering for tuning quantum electronic transport and anisotropy in nanoporous graphene. *J. Am. Chem. Soc.*, 145:8988–8995, Mar 2023.

[MJFDL$^+$20] Alberto Martín-Jiménez, Antonio I. Fernández-Domínguez, Koen Lauwaet, Daniel Granados, Rodolfo Miranda, Francisco J. García-Vidal, and Roberto Otero. Unveiling the radiative local density of optical states of a plasmonic nanocavity by STM. *Nature Communications*, 11, Feb 2020.

[MVVS$^+$18] César Moreno, Manuel Vilas-Varela, Ane Sarasola, Diego Peña, Aran Garcia-Lekue, Aitor Mugarza, Bernhard Kretz, Marius V. Costache, Markos Paradinas, Sergio O. Valenzuela, Gustavo Ceballos, and Mirko Panighel. Bottom-up synthesis of multifunctional nanoporous graphene. *Science*, 360:199–203, Apr 2018.

[PGB20] Alberto Pascual-García and Thomas Bell. Community-level signatures of ecological succession in natural bacterial communities. *Nature Communications*, 11:2386, 2020.

[PZCRdC$^+$24] Ignacio Piquero-Zulaica, Eduardo Corral-Rascón, Xabier Diaz de Cerio, Alexander Riss, Biao Yang, Aran Garcia-Lekue, Mohammad A. Kher-Elden, Zakaria M. Abd El-Fattah, Shunpei Nobusue, Takahiro Kojima, Knud Seufert, Hiroshi Sakaguchi, Willi Auwärter, and Johannes V. Barth. Deceptive orbital confinement at edges and pores of carbon-based 1D and 2D nanoarchitectures. *Nat Commun*, 15:1062, Feb 2024.

[ROC$^+$19] Jesús Redondo, Lukáš Ondič, Aleš Cahlík, Jiří Doležal, Pablo Merino, and Martin Švec. Charge carrier injection electroluminescence with CO-functionalized tips on single molecular emitters. *ACS Nano*, 19:8605–8611, Nov 2019.

[SC94] Paul Solomon and Frank Canora. *Semiconductors and Semimetals.* ScienceDirect, August 1994.

[Sch24] Johannes Schust. Atomically resolved luminescence in a scanning tunneling microscope. Master's thesis, Universität Stuttgart, Germany, Feb 2024.

[SDR05] A. Singha, P. Dhar, and Anushree Roy. A nondestructive tool for nanomaterials: Raman and photoluminescence spectroscopy. *American Journal of Physics*, 73:224–233, Mar 2005.

[SKM+16] Weitao Su, Naresh Kumar, Sandro Mignuzzi, Jason Crain, and Debdulal Roy. Nanoscale mapping of excitonic processes in single-layer MoS_2 using Tip-enhanced Photoluminescence Microscopy. *The Royal Society of Chemistry*, 8:10564–10569, Apr 2016.

[Sto11] Mark I. Stockman. Nanoplasmonics: past, present, and glimpse into future. *Opt. Express*, 19:22029–22106, Oct 2011.

[TSB+13a] Philipp Tonndorf, Robert Schmidt, Philipp Böttger, Xiao Zhang, Janna Börner, Andreas Liebig, Manfred Albrecht, Christian Kloc, Ovidiu Gordan, Dietrich R. T. Zahn, Steffen Michaelis de Vasconcellos, and Rudolf Bratschitsch. Photoluminescence emission and Raman response of monolayer MoS_2, $MoSe_2$, and WSe_2. *Optical Society of America*, 21:4908–4916, Feb 2013.

[TSB+13b] Philipp Tonndorf, Robert Schmidt, Philipp Böttger, Xiao Zhang, Janna Börner, Andreas Liebig, Manfred Albrecht, Christian Kloc, Ovidiu Gordan, Dietrich R. T. Zahn, Steffen Michaelis de Vasconcellos, and Rudolf Bratschitsch. Photoluminescence emission and Raman response of monolayer MoS_2, $MoSe_2$, and WSe_2. *Optics Express*, 21:4908–4916, Feb 2013.

[Voi15] Bert Voigtländer. *Scanning probe Microscopy*. Springer US, August 2015.

[YCG+20] Ben Yang, Gong Chen, Atif Ghafoor, Yufan Zhang, Yao Zhang, Yang Zhang, Yi Luo, Jinlong Yang, Vahid Sandoghdar, Javier Aizpurua, Zhenchao Dong, and J. G. Hou. Sub-nanometre resolution in single-molecule photoluminescence imaging. *Nature Photonics*, 14:693–699, Nov 2020.

[YWZ+20] Wei Yu, Zishen Wang, Xiaoxu Zhao, Junyong Wang, Tun Seng Herng, Teng Ma, Zhiyu Zhu, Jun Ding, Goki Eda, Stephen J. Pennycook, Yuan Ping Feng, and Kian Ping Loh. Domain engineering in ReS_2 by coupling strain during electrochemical exfoliation. *Advanced Functional Materials*, 30:2003057, Jun 2020.

[ZFR+06] O. H. Y. Zalloum, M. Flynn, T. Roschuk, J. Wojcik, E. Irving, and P. Mascher. Laser photoluminescence spectrometer based on charge-coupled device detection for silicon-based photonics. *Review of Scientific Instruments*, 77, Feb 2006.

[Zha21] Minghao Zhang. Scanning tunneling microscopy and Raman spectroscopy in 1t-tase$_2$. Master thesis, Technische Universität München, Garching, Germany, May 2021.

[ZSWS16] Zhenglong Zhang, Shaoxiang Sheng, Rongming Wang, and Mengtao Sun. Tip-enhanced Raman spectroscopy. *ACS Nano*, 88:9328–9346, Aug 2016.

A Focused Ion Beam (FIB)

Focused Ion Beam (FIB) has become a UHV *in-situ* technique for the fabrication, modification and characterization of STM tips at the nanoscale [FIB16]. As the ion beam strikes the tip, the incident ions interact with the material atoms, cleaning and sharpening the tip in a controlled manner. However, it also has several drawbacks, like introducing defects, depending on the nature and the energy of the ion.

In the experiments presented in the results, 25 μm-thin Ag tips made by focused Xe^+ were used. Xe, being a noble gas, is inert and its larger mass reduces the penetration depth into the material. After initial sharpening, the tips underwent Ar^+ sputtering under UHV conditions, before being in-situ transferred into the SPM head [dCFSD⁺24]. Ar ions, whose mass is much lower compared to Xe, have a shallower penetration depth, allowing for more precise material removal at the tip apex. This finer control over the tip shaping process enables to achieve a high level of precision and sharpness.

B Near-Field coupling

The Gaussian-Lorentzian convolution [JBLF18] is given by

$$GLP(x,\mu,\sigma,A) = \frac{A}{1+4m\frac{(x-\mu)^2}{\sigma^2}} e^{-4\ln 2(1-m)\frac{(x-\mu)^2}{\sigma^2}}, \tag{9}$$

where μ represents the mean, σ the standard deviation, A the amplitude and m the weight between a pure Gaussian (m=0) and a pure Lorentzian (m=1) distributions.

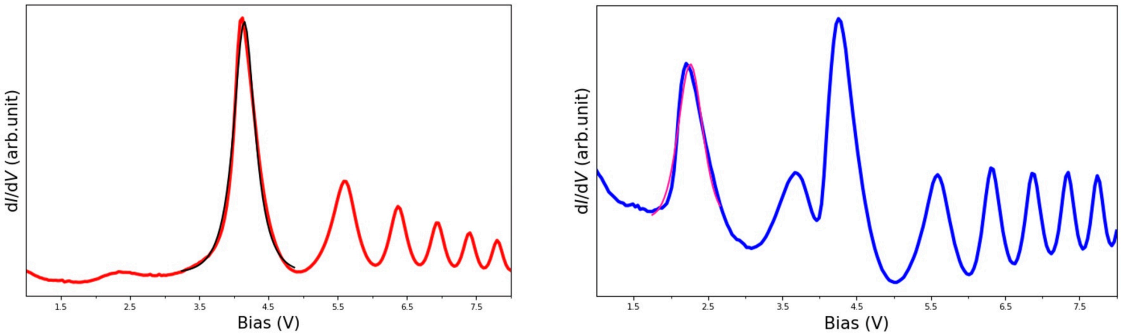

(a) (b)

Figure 21: FERs, measured as dI/dV at constant current feedback with an Ag tip covered by Au on a clean Ag(111) surface sample, with Gaussian-Lorentzian fits. **(a)** Without the illumination source. (**b**) With illumination source. The first blue peak corresponds to the converted electrons, while the third one represents mostly the remaining non-converted electrons for the first (red) peak in the absence of the laser. Current set-point: 200pA, Lock-in modulation amplitude: 50mV.

Peak	μ	σ	A	m
Red	4.15	0.39	160.43	0.87
Blue	2.26	0.56	24.95	0

Table 3: Parameters for the Gaussian-Lorentzian fit for the FERs peaks in Figure 21.

C Setting up a PSTM

The laboratory acquired an RHK STM microscope upgraded with a fixed lens system at the cryostat for STML/TEPL experiments, yet to be commissioned. It has never been fully operational due to large topographic noise and communication problems between the PC and High-Voltage (HV) supply and control of the piezo actuators. The project has been restarted through this thesis to reassemble and upgrade it with an optical setup to perform PSTM.

The RHK microscope is refrigerated by a closed-cycle He cryostat, which was tested to reach a temperature of 9 K (Figure 23). In addition, other tasks were done, such as the coupling of the optical setup to the LT-STM UHV chamber for collecting/inserting light from the tunnelling junction. The communication problem was also resolved by replacing the RHK SHARC/DSP and the PMC Interface boards. In addition, clean Au on mica samples and Au tips (section 3.1.1) were prepared to begin STM experiments and, consequently, to address noise issues during scanning and possibly achieve atomic resolution. To clean the samples, a flame annealing in air was done, *i.e.*, the samples were heated from behind the plate using a torch.

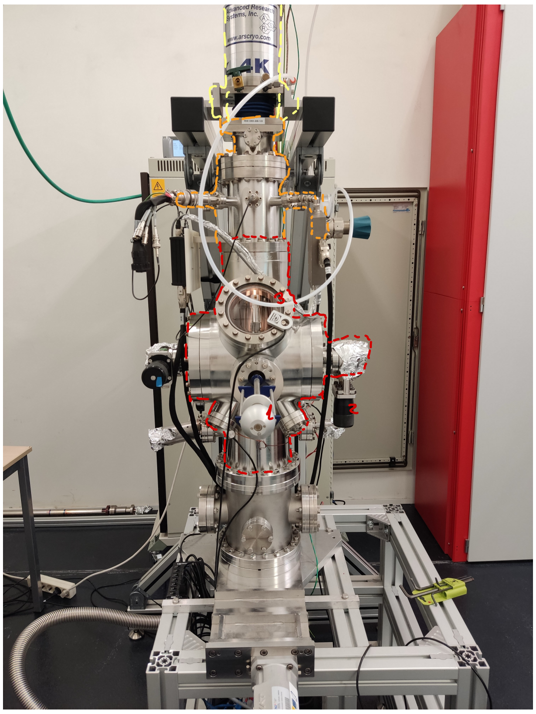

Figure 22: A variable temperature, closed cycle RHK scanning tunneling and force microscope which operates between 10K and 400K.

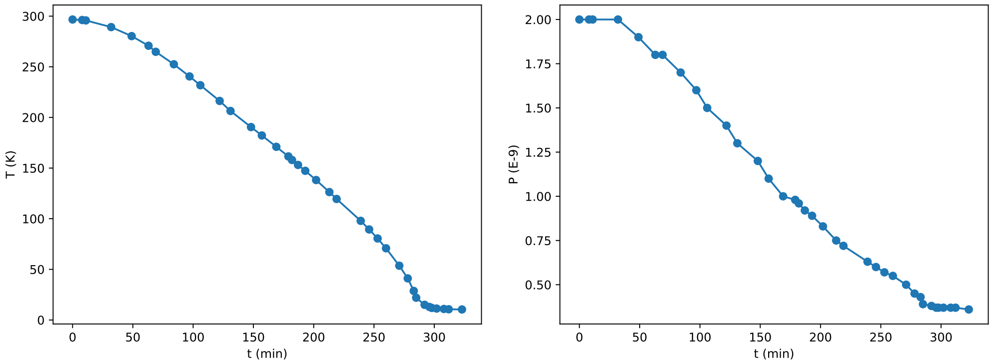

(a)

(b)

Figure 23: Test RHK cool system. **(a)**Temperature evolution of the STM chamber with respect to time.**(b)**Pressure evolution of the STM chamber with respect to time.

C.1 Manipulator

The preparation chamber consists of a complementary UHV chamber connected to the STM chamber, used for in-situ preparation of samples before measuring. It is designed to host multiple preparation sample tools, like ion-sputtering guns, metal or organic evaporators, *etc.*, and requires a manipulator that can hold and position the sample for the different preparation treatments it may undergo. To accomplish this, a previously unused and unassembled manipulator was proposed for use, which required adaptation to a worn-out heating stage that was missing the filament for applying high voltage to heat the sample up to 2000 K. Both instruments were mechanically coupled to ensure good thermal contact between the cooper body of the heating stage that has to be refrigerated (see the cooling tubes in Figure 24), if needed, and the main manipulator body. The filament was reconstructed using a 250 μm thin W wire attached to two pins with newly polished ceramics. Finally, the entire setup was cleaned using an ultrasonic bath to make it compatible with the ultra-clean conditions of UHV, 20 minutes of acetone to remove organic contaminants plus 20 minutes of ethanol to remove acetone residue.

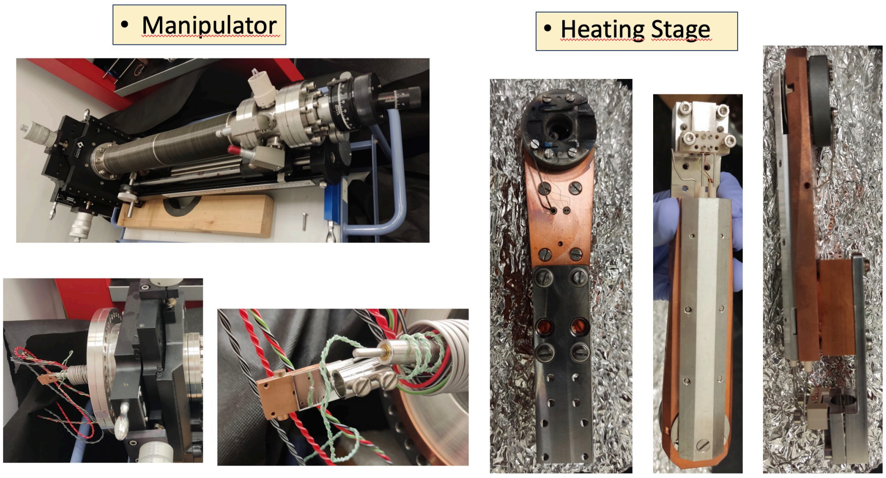

Figure 24: Initial state of the manipulator and the heating stage.

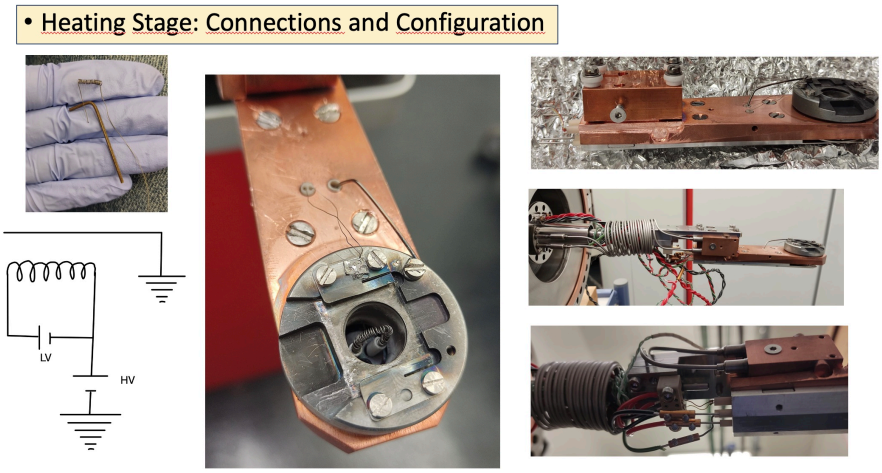

Figure 25: Repair of the heating stage and its adaptation to the manipulator.

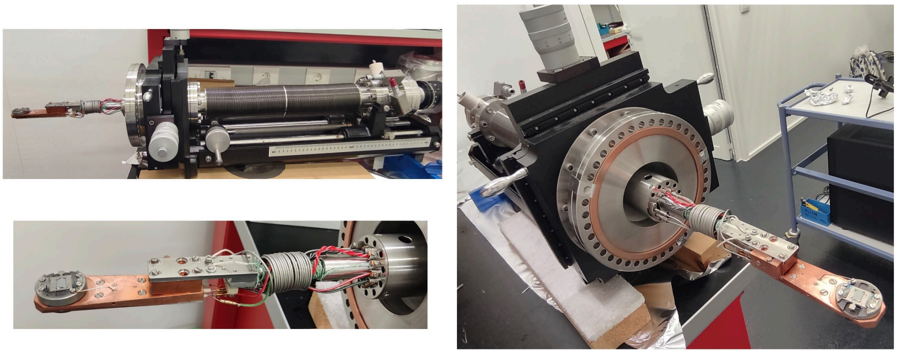

Figure 26: Final state of the manipulator and the heating stage.

C.2 Calibration of STM Axes

This section describes the calibration of the piezoelectric response in X, Y and Z directions at 10 K using a reference sample of Au in mica. The calibration of an STM is essential for ensuring accurate measurements. Calibration factors, the ratio between a reference value and the one measured with the equipment, obtained in this analysis are summarized in Table 4. Used reference parameters: the height of an Au step and the parameter of the Au(111) atomic lattice.

C.2.1 X-Y piezo calibration

Au crystallizes following a face-centered cubic structure so, assuming the same degree of distortion within the X and Y axis (*i.e.*, in-plane), calibrating one should be equivalent to calibrating the other.

STM topographic image in Figure 27**(a)** presents a hexagonal arrangement of pseudo-circular protrusions, only visible within an area of a few nanometers in size. It shows a periodicity of 3.00 Å and corrugation of about 20 pm, as measured from the line profile taken along one of the high symmetry axis (Figure 27**(b)**). These values are in good agreement with the atomic constant of the hexagonal Au(111) lattice (2.88 Å) and typical values of atomic corrugation measured by STM. It confirms that each of the observed protrusions corresponds to one single Au atom of the Au(111) surface. Tip changes above or below the described region prevented observation of further repetitions of the Au(111) unit cell.

C.2.2 Z piezo calibration

STM topographic image in Figure 28**(c)** presents two atomically flat Au(111) terraces. Two different methods will be employed for calibration in the z direction:

1. Topographic line profile: Selecting a line of N pixels across the Au step to measure the apparent heights along the x-direction (Figure 28**(a)**).
2. Histogram Method: The software creates a height histogram of a region N×N pixel area containing the step. This displays two peaks related to the upper and lower parts of the step. The center of the Gaussian fits provides the mean distribution heights, from which the step is calculated. As this method considers more data points for calculations, it should offer more reliable results than the first one (Figure 28**(b)**).

	Measured Distance (Å)	Literature Distance (Å)	Calibration factor
Z Method 1	2.69	2.36	0.877
Z Method 2	2.37		0.996
X-Y	3.00	2.88	0.961

Table 4: Calibration factors for different axes.

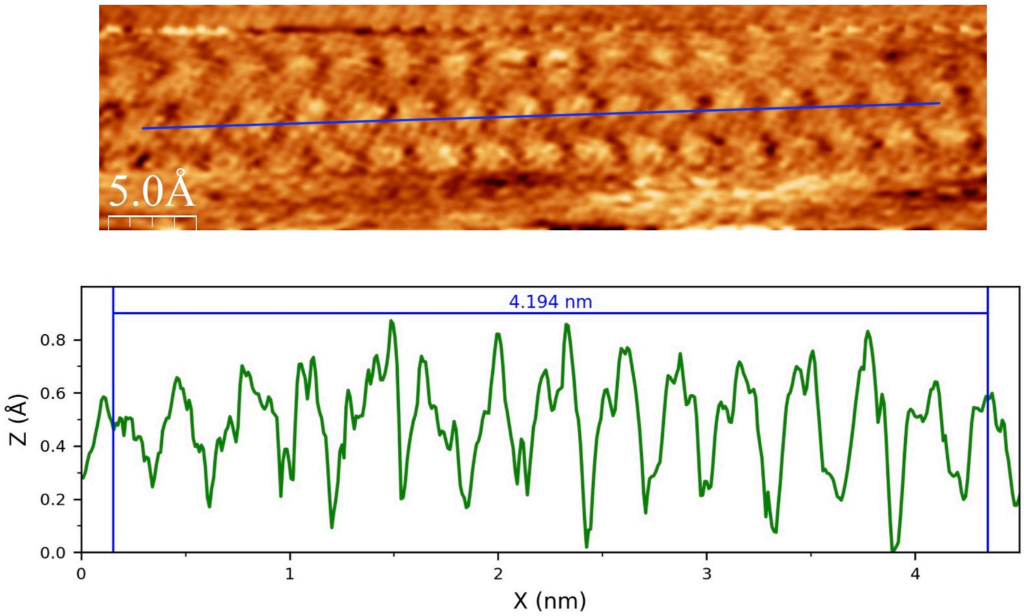

Figure 27: X-Y Axis Piezos Calibration. **(a)** STM image with atomic resolution of a clean Au on mica sample, annealed previously in air. **(b)** Topographic line profile of the blue line marked region relative to the x-axis. Each protrusion correspnds to an Au unit cell. Temperature: 9.3K. Pressure: $2{\cdot}10^{-10}$ mbar.

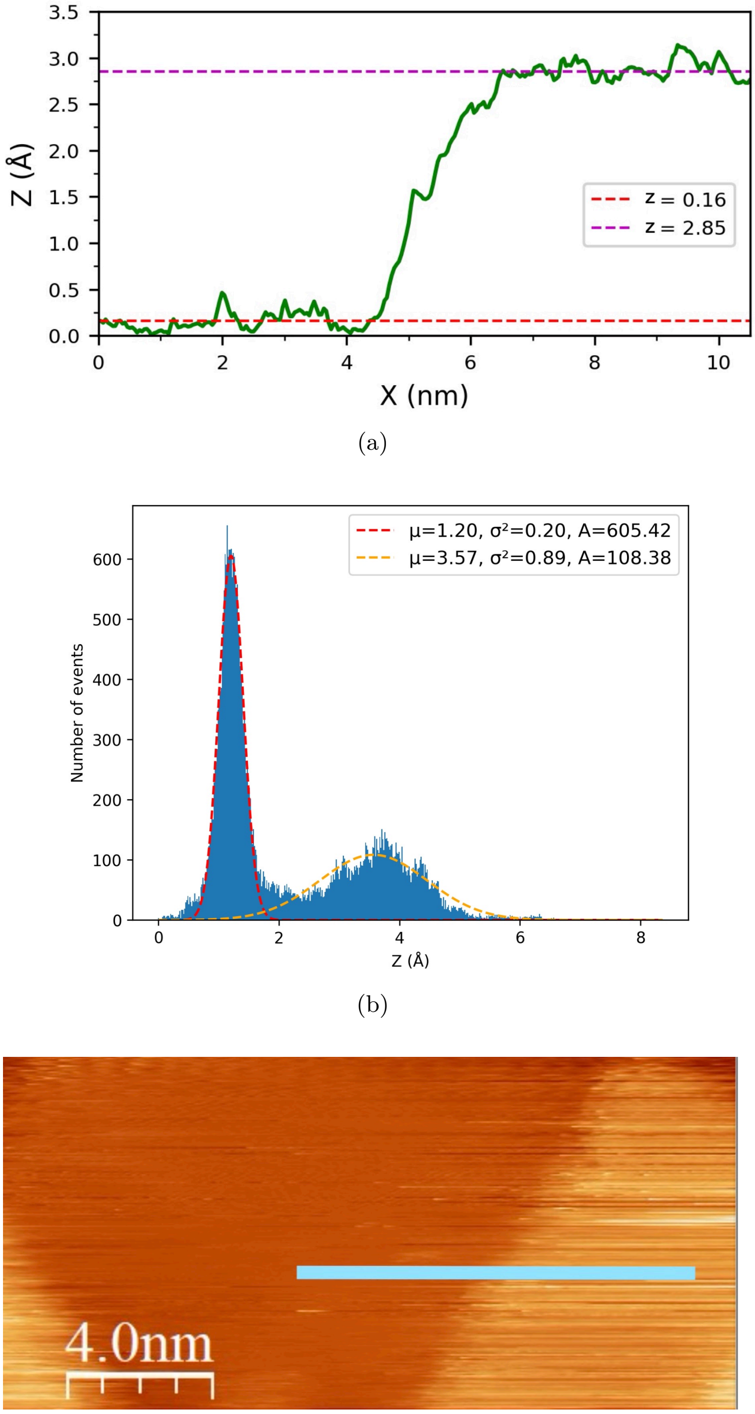

(a)

(b)

(c)

Figure 28: Z axis calibration using an Au on mica sample. **(a)** Topography height of the blue-marked line relative to the x-axis. To obtain the step height, the mean z components for both the upper and lower regions are calculated, resulting in a step height of 2.69 Å. **(b)** Height histogram of a clean Au surface MxM pixel region containing the step edge. The two peaks correspond to the accumulation of events in the upper and lower parts of the step. Gaussian fits provide the mean distributions, leading to a step height of 2.37 Å.**(c)** STM image with atomic resolution. Temperature: 9.3K. Pressure: 10^{-10} mbar.

D Support Images

D.1 STM tips

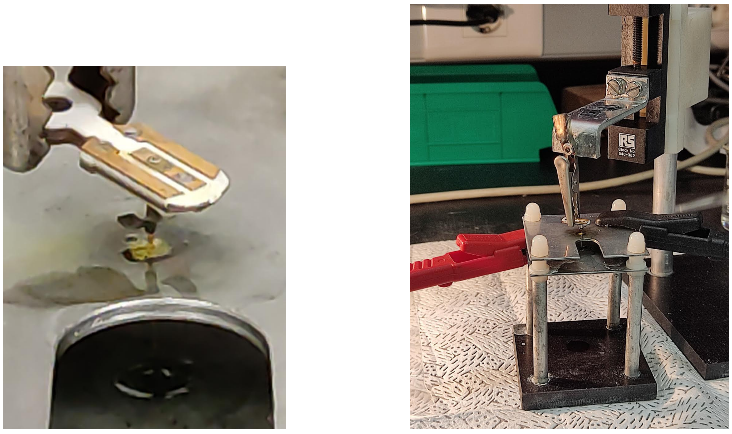

(a)

(b)

Figure 29: Tip etching setup.

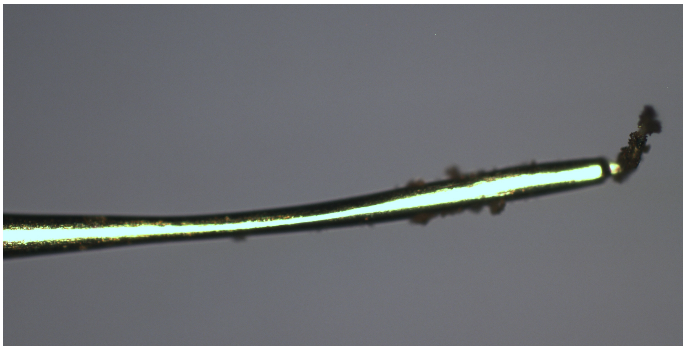

Figure 30: Failed tip-etching attempt with residual oxidation in the surface due to an excess of diluent in the etching solution. Voltage : 3.5V, Time: 75 min, Etchant: HCl 37%, Diluent: Ethanol. Solution: 50% HCl, 50% Ethanol.

D.2 MoSe$_2$ images

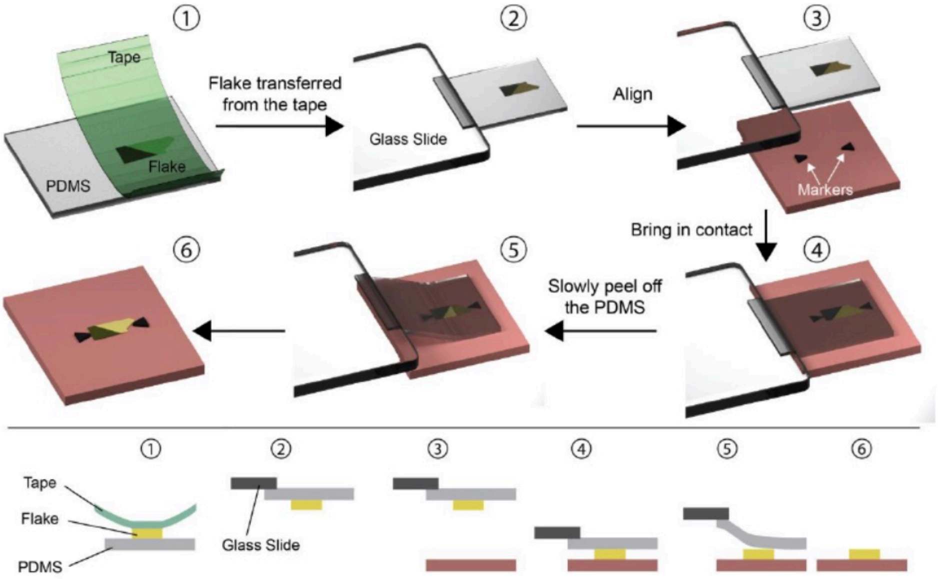

Figure 31: PDMS transfer method: **1)** The flake is exfoliated onto a PDMS stamp. **2)** The stamp is attached to a glass slide connected to a micromanipulator. **3)** and **4)** The flake is aligned with the substrate using a microscope and brought in contact. **5)** and **6)** After peeling of the PDMS, the flake is deposited on the substrate. Image taken from [FNMG+17].

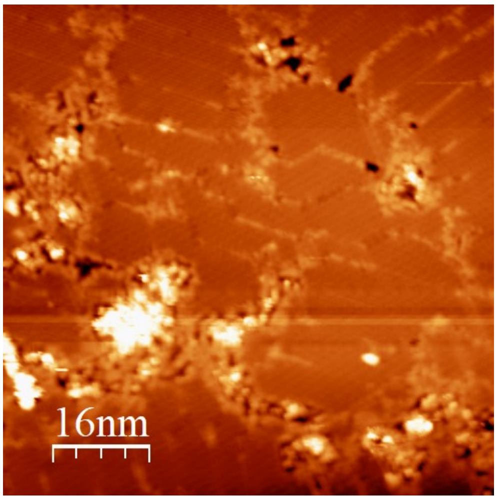

(a)

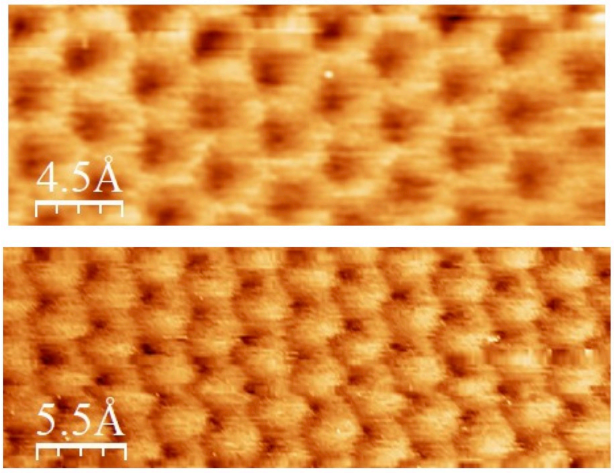

(b)

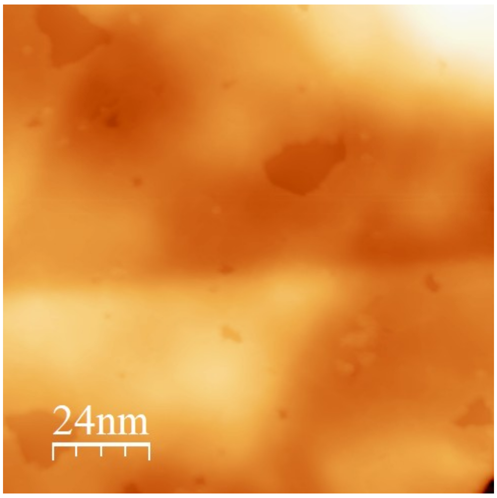

(c)

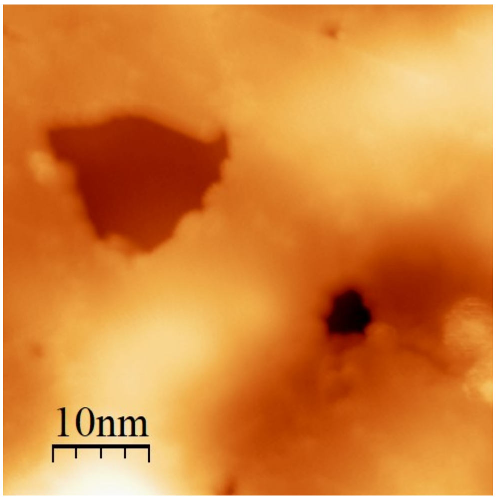

(d)

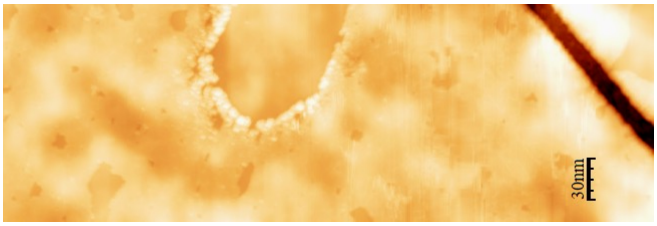

(e)

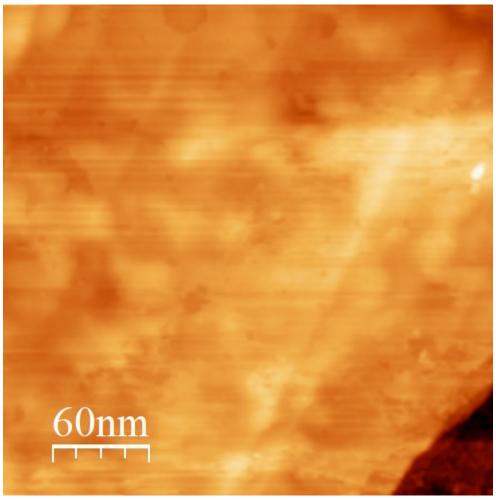

(f)

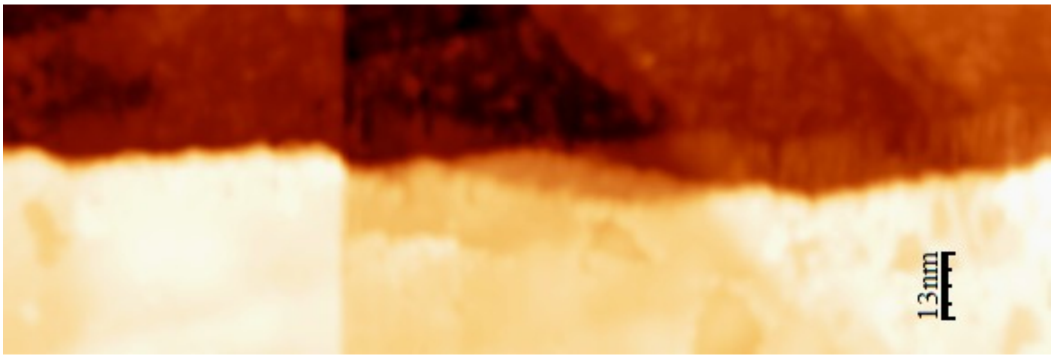

(g)

Figure 32: STM topographic images of flake 12: $MoSe_2$ on NPG on Au(111) after 3 hours of annealing at 250°. **(a)** $MoSe_2$ terrace displaying twin boundaries and 3D-like contaminants (likely of PDMS-origin). **(b)** Lattice structure of the TMD with atomic resolution. The contrast-inversion between the two images is due to changes at the tip apex. **(c)**,**(e)** and **(d)** $MoSe_2$ clean region showing surface undulations/bubbles. **(f)** $MoSe_2$ clean region with apparent Au steps. **(g)** Region where the PL spectra was recorded.